ADVANCES IN INORGANIC CHEMISTRY AND RADIOCHEMISTRY, VOL. 27

ELECTRON-DENSITY DISTRIBUTIONS IN INORGANIC COMPOUNDS

KOSHIRO TORIUMI* and YOSHIHIKO SAITO†

*Institute for Molecular Science, Okazaki, Japan and †Department of Chemistry, Faculty of Science and Technology, Keio University, Hiyoshi, Kohoku-ku, Yokohama, Japan

I. Introduction 28
II. Electron-Density Distributions Determined by X-Ray Diffraction Methods 28
A. The Relationship between the Electron-Density Distribution in a Crystal and the X-Ray Scattering Amplitudes from a Single Crystal 28
B. Deformation Density 29
C. Experimental Errors 31
III. 3*d* Electron-Density Distributions 33
A. Transition Metal Complexes 33
B. Transition Metal Complexes Having Short Metal–Metal Bonds . . 46
C. Organometallic Compounds 54
IV. Net Charges of Transition Metal Atoms 64
A. Estimation of Net Charges of Atoms 65
B. Net Charges of Transition Metal Atoms 68
C. 3*d* Electron Populations in Each Atomic Orbital Placed in a Ligand Field 70
D. Formal Oxidation States of Transition Metal Atoms 71
V. Chemical Bonds between Transition Metal Atoms and Ligating Atoms 72
A. Ionic Bonds 72
B. Coordination Bonds 73
C. Covalent Bonds 75
D. Chemical Bonds in π-Complexes 76
VI. Electron-Density Distributions in Some Inorganic Crystals 76
Aspherical Electron Distributions in Metal Crystals 76
VII. Concluding Remarks 79
References 79

ISBN 0-12-023627-3

I. Introduction

This article comprises a survey of electron-density studies of inorganic compounds. The compounds included are transition metal complexes, minerals such as oxides, sulfides, and spinels, organometallic compounds, and metals. The measurement of electron density in inorganic compounds is a developing field. Studies of compounds containing heavy atoms lag somewhat behind those of organic compounds consisting of first-row atoms (*14*, *20*). A remarkable development in this field in the past decade is that the asphericity of $3d$ electron distribution in transition metal compounds has been established. Results obtained in recent years indicate that experimental densities are a sensitive test of theoretical methods. Molecular wave functions have conventionally been calculated to obtain molecular energy levels, but now they can be directly compared with the spatial distribution of electrons.

It is not our intention in this article to give a comprehensive review of electron-density studies of inorganic compounds but to describe the characteristic behavior of $3d$ electrons in molecules and to illustrate how the nature of the bonding in inorganic compounds is reflected in experimental densities.

II. Electron-Density Distributions Determined by X-Ray Diffraction Methods

A. The Relationship between the Electron-Density Distribution in a Crystal and the X-Ray Scattering Amplitudes from a Single Crystal

At present the X-ray diffraction method is used mostly to determine atomic positions in a crystal. However, X-ray scattering amplitudes depend directly on the electron-density distribution in a crystal, from which atomic positions can be derived on the assumption of coincidence of the nuclear positions and the center of gravities of total electron densities around atomic nuclei.

The scattering amplitude is given by the absolute value of the following expression, which is a Fourier transform of the total electron-density distribution in a unit cell and is called a crystal structure factor:

$$F(\mathbf{H}) = \int_{\text{unit cell}} \rho(\mathbf{r}) \exp(2\pi i \mathbf{H} \cdot \mathbf{r}) d\tau \tag{1}$$

where $\mathbf{r}$ is a vector defining a position in real space and $\mathbf{H}$ is a reciprocal lattice vector. The electron density $\rho(\mathbf{r})$ at a position $\mathbf{r}$ in the unit cell is given by the inverse Fourier transform,

$$\rho(\mathbf{r}) = (1/V) \sum_{\mathbf{H}} F(\mathbf{H}) \exp(-2\pi i \mathbf{H} \cdot \mathbf{r}) \tag{2}$$

where a summation is made over all the reciprocal lattice points, and V is the unit cell volume. Equation (2) shows that the electron-density distribution in a crystal can be obtained by accurate measurement of the structure amplitudes. However, Eq. (1) implies that the structure factor is generally a complex quantity: it gives us the amplitude and phase of the scattered wave from the unit cell. $\rho(\mathbf{r})$ can be rewritten as follows:

$$\rho(\mathbf{r}) = (1/V) \sum_{\mathbf{H}} |F(\mathbf{H})| \exp(2\pi i \mathbf{H} \cdot \mathbf{r} - i\alpha_{\mathbf{H}}) \tag{3}$$

where $|F(\mathbf{H})|$ is the amplitude and $\alpha_{\mathbf{H}}$ is the phase angle. $|F(\mathbf{H})|$ can be obtained directly from the measured intensity of reflections, whereas the phase angle $\alpha_{\mathbf{H}}$ cannot be measured directly, but is evaluated from the calculated structure factor $F_c(\mathbf{H})$ derived from a model electron density distribution in the crystal, after the crystal structure analysis has been completed.

For centrosymmetric crystal structures, $F(\mathbf{H})$ takes a simpler form:

$$F(\mathbf{H}) = \int_{\text{unit cell}} \rho(\mathbf{r}) \cos(2\pi \mathbf{H} \cdot \mathbf{r}) d\tau \tag{4}$$

In this case, the phase problem reduces to a question of the sign of the structure factor. Since the sign of the structure factor can be evaluated more reliably than the phase angle, the electron density in a centrosymmetric crystal can be evaluated more accurately than that in an acentric crystal (*93*). Equation (2) implies that total, time-averaged electron density can be determined by the diffraction method.

B. Deformation Density

Valence electron density, containing chemically important information, is relatively small compared to the total electron density. Electron-density changes due to molecular formation, i.e., charge migration and charge accumulation, are small in magnitude compared to the

total electron density. Thus, a more sensitive function must be introduced to obtain chemical information from the observed electron density. A suitable function can be obtained by subtracting all the unperturbed spherical atom density from the total electron density:

$$\Delta\rho(\mathbf{r}) = \rho(\mathbf{r}) - \sum_{\text{all atoms}} \rho_{j,\,\text{spherical atom}}(\mathbf{r} - \mathbf{r}_j) \tag{5}$$

where $\rho(\mathbf{r})$ is the total electron density at a point $\mathbf{r}$ in space, and $\rho_{j,\,\text{spherical atom}}$ stands for the unperturbed, spherically averaged atom densities located at the same position, $\mathbf{r}_j$, in space. A sum in Eq. (5) is called promolecule (*35*), which gives an imaginary electron density constructed by superposition of free atoms placed at their molecular geometry. Since $\Delta\rho(\mathbf{r})$ represents the deformation density from spherical atom density upon molecular formation, it is referred to as the "deformation density." Unperturbed spherical atom density is generally taken as the spherically averaged ground state atom density. From Eqs. (1) and (2), the deformation density can be calculated from a function of observed and calculated structure amplitudes,

$$\Delta\rho(\mathbf{r}) = (1/V) \sum_{\mathbf{H}} [F_0(\mathbf{H}) - F_c(\mathbf{H})] \exp(-2\pi i \mathbf{H} \cdot \mathbf{r}) \tag{6}$$

This function is known as the difference Fourier synthesis. Calculated structure amplitudes, $F_c(\mathbf{H})$, can be derived by the Fourier transform of the second term in Eq. (5) as

$$F_c(\mathbf{H}) = \sum_j f_j T_j \exp(2\pi i \mathbf{H} \cdot \mathbf{r}_j) \tag{7}$$

where f_j and T_j are the atomic scattering factor and temperature factor of the jth atom, respectively. Atomic scattering factors have been calculated by the Fourier transform of the spherically averaged ground state density, $\rho_j(\mathbf{r})$.

Molecular geometry, namely, each atomic position $\mathbf{r}_j$ in the unit cell, is conventionally determined by the least-squares fitting method based on the residue between $|F_0|$ and $|F_c|$. A simple least-squares technique used in the conventional crystal structure analysis gives a slightly biased atomic position, because of the aspherical electron-density distribution caused by the chemical environment (*15*, *18*). To obtain the unbiased deformation density, the atomic positions are commonly de-

termined by the neutron diffraction method (*13, 21*) or the least-squares calculation based on the high-angle X-ray reflections [high-angle refinement (*21, 79*)]. These techniques are based on the scattering from the atomic nuclei or the undeformed core electrons, respectively.

C. Experimental Errors

If we wish to discuss the chemical properties derived from the observed deformation densities, it is obviously essential that the experimental errors should be estimated. This subject has been discussed in detail in a number of publications (*13, 17, 26, 27, 51, 61, 73*). Thus, only the main sources and magnitudes of the experimental errors necessary for proper assessments of the results will be described here. Experimental errors may be divided into systematic and statistical errors, and statistical errors will be treated first. As discussed in the previous section, the deformation density is defined as

$$\Delta\rho = (1/k)\rho_{\text{obs}} - \rho_{\text{calc}} \tag{8}$$

where k is a scale factor for the observed structure amplitudes. The estimated errors of the observed deformation density can be calculated by the variances (squares of estimated standard deviations) and covariances of each term (*61, 73*)

$$\begin{aligned}\sigma^2(\Delta\rho) = {} & (1/k^2)\sigma^2(\rho_{\text{obs}}) + (\rho_{\text{obs}}/k)^2[\sigma(k)/k]^2 \\ & + \sigma^2(\rho_{\text{calc}}) + \text{cov}(\rho_{\text{obs}}/k, \rho_{\text{calc}})\end{aligned} \tag{9}$$

The fourth term representing the covariances arises from the correlations between the errors of ρ_{obs} and the atomic parameters, on which ρ_{calc} is based, calculated in the least-squares refinement. The first term in Eq. (9) can be expressed as a function of the error of the observed structure amplitudes, $\sigma(|F_0|)$. By means of Eq. (3), $\sigma^2(\rho_{\text{obs}})$ can be given approximately as follows:

$$\sigma^2(\rho_{\text{obs}}) = (1/V^2) \sum_{\text{indep } \mathbf{H}} \sigma^2(|F_0|) \left\{ \sum_{\text{form}} \cos(2\pi \mathbf{H}_f \cdot \mathbf{r} - \alpha_{\mathbf{H}_f}) \right\}^2 \tag{10}$$

where the first summation is carried out over the independent reflections only and the second over all the symmetry-related reflections (*27*). The errors of observed structure amplitudes, $\sigma(|F|)$, are generally

estimated based on the discrepancies among the symmetry-related reflections (*1*) as follows:

$$\sigma^2(|F|) = \sigma^2_{\text{count. statistics}} + (a \cdot |F|)^2 \tag{11}$$

where the first term represents the error due to counting statistics. The discrepancy parameter of a is generally estimated to be 0.010–0.015 in accurate measurements. When symmetry-related reflections are measured for n times, $\sigma(|F_0|)$ reduces to $\sigma(|F_0|)/\sqrt{n}$. Other three terms in Eq. (9) are essentially related to the accuracy of the least-squares refinement, and estimated from the errors of a scale and atomic parameters calculated in the refinement. Detailed analyses of these four contributions have been carried out in several publications (*17, 51, 61, 72, 73*). Therefore, only the general features of the errors will be mentioned here. Error in the deformation density caused by $\sigma(\rho_{\text{obs}})$ is fairly constant over the unit cell, except in the vicinity of crystallographic symmetry elements where $\sigma(\rho_{\text{obs}})$ becomes two or three times as large as that for the general position. However, the errors in the positional and thermal parameters employed to obtain ρ_{calc} and of the scale factor have serious influence within about 0.3 Å of the nuclear positions (*78*). In current work, errors near the atomic positions are exceptionally large, and no significant information can be attached to the observed deformation density at the nuclear positions. Usually values of $\sigma(\Delta\rho)$ with good quality data presently obtainable are constant over the unit cell with the order of 0.1–0.2 e Å^{-3}. If the deformation density is averaged over the chemically equivalent portions in a molecule, the error will be reduced to about 0.05 e Å^{-3}.

Deformation density occasionally suffers from the systematic errors in the atomic parameters caused by crystallographic problems and the technique of least-squares refinement. A conventional least-squares technique rarely gives the true atomic parameters because the valence electron densities around the atomic nuclei are generally deformed upon molecular formation and their centers of gravities do not coincide in position with the atomic nuclei (*15, 28*): charge accumulation due to lone-pair or bonding orbitals displaces the center of gravity of total electron density from the atomic nucleus. Unbiased parameters can be obtained from a single crystal neutron diffraction experiment (*13, 21*). Useful results may also be obtained with the high-order refinement based on high-angle X-ray data only (*21, 79*), making the reasonable approximation that valence electron density is diffused and contributes to the low-angle reflection data only. Other crystallographic sources of systematic errors are the primary or the secondary extinc-

tion effect, multiple reflections, and thermal diffuse scattering. Readers may refer to various publications on these subjects, for example, extinction effect (*8, 18, 94*), multiple reflections (*83*), and thermal diffuse scattering (*70*).

All these errors can be properly corrected by appropriate corrections and experimental techniques (*92*), (e.g., low-temperature measurement and measurement of symmetry-related reflections). In particular, low-temperature measurements are essential to reduce the thermal smearing of the deformation density due to the thermal vibration of atoms.

III. 3*d* Electron-Density Distributions

In 1973, Iwata and Saito determined the electron-density distribution in crystals of $[Co(NH_3)_6][Co(CN)_6]$ (*37*). This was the first determination of electron density in transition metal complexes. In the past decade, electron-density distributions in crystals of more than 20 transition metal complexes have been examined. Some selected references are tabulated in Table I. In most of the observed electron densities, aspherical distributions of 3*d* electron densities have been clearly detected in the vicinities of the metal nuclei. First we shall discuss the distributions of 3*d* electron density in the transition metal complexes. Other features, such as effective charge on transition metal atoms and charge redistribution on chemical bond formation, will be discussed in the following sections.

A. Transition Metal Complexes

Most coordination compounds have octahedral, square-planar, or tetrahedral structures. Asphericities of 3*d* electron-density distributions around transition metal atoms placed in an octahedral and tetrahedral environment differ distinctly from each other. Thus, they will be dealt with separately.

1. Transition Metal Atoms in Octahedral Environments

a. $[Co(NO_2)_6]^{3-}$. Geometries around the transition metal atoms in the crystals listed in Table I are mostly octahedral, but are more or less deformed from a regular octahedron. We illustrate the electron-density distribution in crystals of $K_2Na[Co(NO_2)_6]$ (*59*), in which a cobalt atom

TABLE I

SOME SELECTED MEASUREMENTS OF ELECTRON-DENSITY DISTRIBUTIONS IN CRYSTALS OF TRANSITION METAL COMPLEXES

Crystal	Space group	Number of d electrons	Ligand field[a]	Reference
$K_2Na[Co(NO_2)_6]$	$Fm3$	6	O_h	*59*
$[Co(NH_3)_6][Co(CN)_6]$	$R\bar{3}$	6	D_{3d}	*37*
$[Co(NH_3)_6][Cr(CN)_6]$	$R\bar{3}$	6(Co), 3(Cr)	D_{3d}	*38*
FeS_2	$Pa3$	6	D_{3d}	*74, 75*
$[Rh(R,R\text{-chxn})_3](NO_3)_3 \cdot 3H_2O$	$P6_3$	6	D_3	*53*
TiO_2	$P4_2/mnm$	0	D_{2h}	*68*
γ-Fe_2SiO_4	$Fd3m$	6	D_{3d}	*50*
γ-Co_2SiO_4	$Fd3m$	7	D_{3d}	*50*
γ-Ni_2SiO_4	$Fd3m$	8	D_{3d}	*49*
$KMnF_3$	$Pm3m$	5	O_h	*42*
$KCoF_3$	$Pm3m$	7	O_h	*41*
$KNiF_3$	$Pm3m$	8	O_h	*43*
$KCuF_3$	$I4/mcm$	9	D_{2h}	*82*
$CoAl_2O_4$	$Fd3m$	7	T_d	*84*
α-K_2CrO_4	$Pnma$	0	T_d	*85*
$Cr(CO)_6$	$Pnma$	6	O_h	*63, 61*
$(C_6H_6)Cr(CO)_3$	$P2_1/m$	6	C_{3v}	*62*
$[(C_5H_5)Fe(CO)_2]_2$	$P2_1/c$	7	(C_{3v})	*52*
$(\eta^5\text{-}C_5H_5Ni)_2C_2H_2$	$Fm2m$	9	C_s	*90*
$Cr_2(CH_3CO_2)_4 \cdot 2H_2O$	$C2/c$	4	$C_{4v}(D_{4h})$	*10*
$Mo_2(CH_3CO_2)_4$	$P\bar{1}$	4	$C_{4v}(D_{4h})$	*33*
Ti_2O_3	$R\bar{3}c$	1	$C_3(D_{3d})$	*88*
V_2O_3	$R\bar{3}c$	2	$C_3(D_{3d})$	*87*

[a] Symmetry of the ligand field around a transition metal atom. An approximate symmetry is indicated in parentheses.

is coordinated regular octahedrally by six N atoms of NO_2 groups with a Co—N bond distance of 1.9516(7) Å. A transition metal complex with this type of high symmetry is easily accessible for theoretical treatment. A three-dimensional difference-Fourier map around the Co atom is shown in Fig. 1a. This is a deformation density in a section containing a Co—N bond and two threefold axes of the CoN_6 octahedron (Fig. 1b). A remarkable feature appears around the Co atom. Sharp positive peaks of 1.7(1) e Å^{-3} are located on the threefold axes at 0.43 Å from the Co nucleus, and negative troughs of $-0.8(1)$ e Å^{-3} on the fourfold axes at 0.62 Å. In all, eight equivalent positive peaks are arranged at the apices of a cube around the Co nucleus, and six negative troughs at the face centers, as illustrated in Fig. 1c. In an octahedral environ-

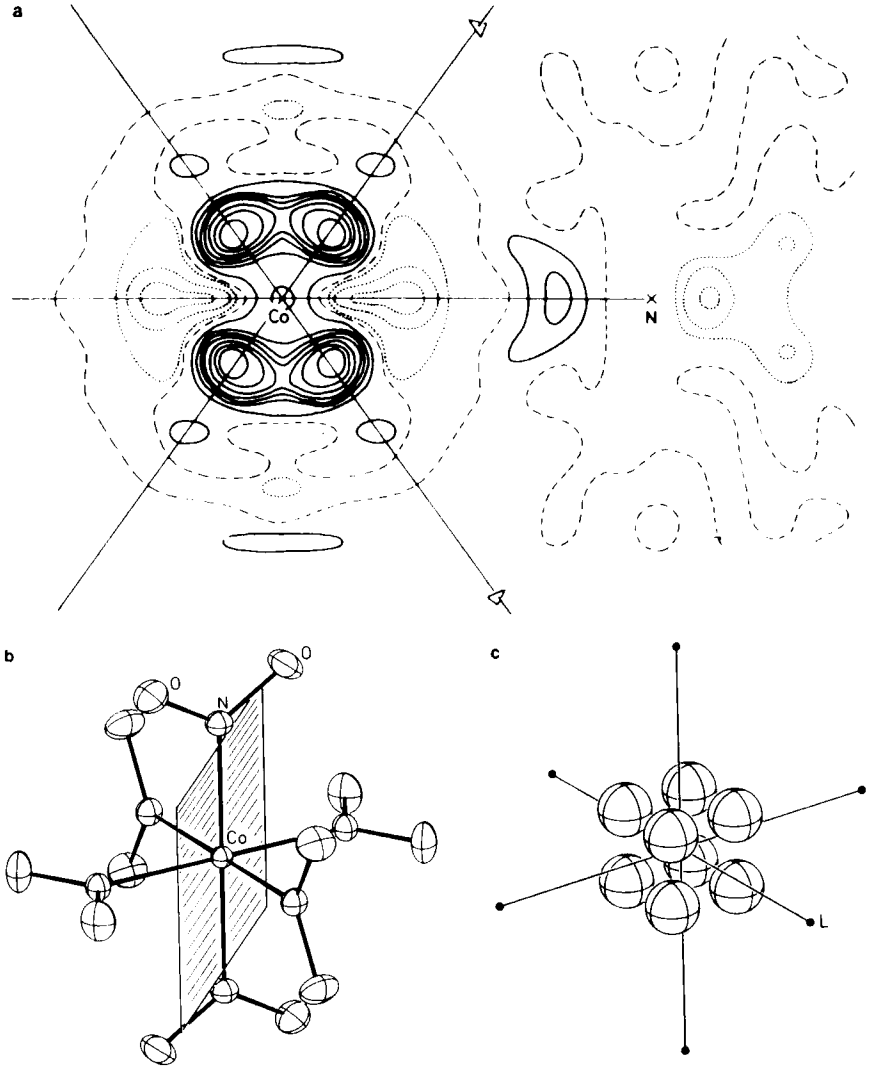

FIG. 1. Observed deformation density of $K_2Na[Co(NO_2)_6]$ (*59*). (a) Deformation density in a section containing a Co—N bond and two C_3 axes, whose plane is shown in (b). Contours are at intervals of 0.2 e Å^{-3}. Negative contours are dotted, zero being chain dotted. (b) Molecular Structure of $[Co(NO_2)_6]^{3-}$, showing the plane in (a). (c) Illustrative view of the arrangement of electron excess regions (t_{2g}).

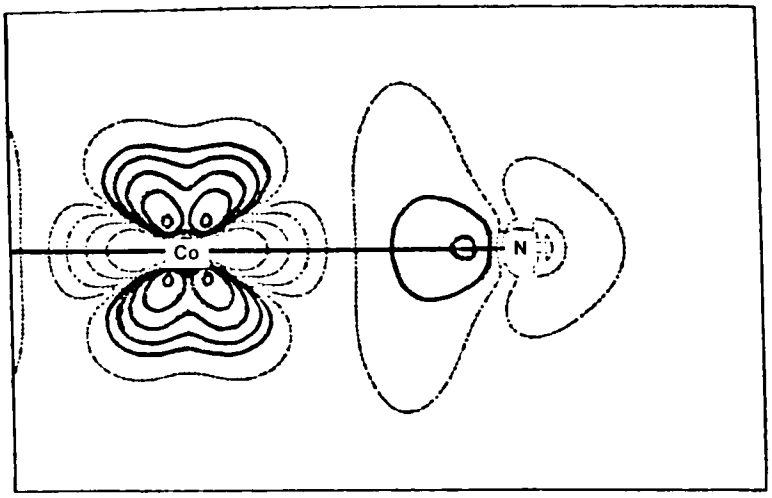

FIG. 2. Theoretical deformation density of $[Co(NO)_2)_6]^{3-}$ in the same section as Fig. 1a (*55*). Contours are ±0.3, ±0.7, ±1.4, ±2.7, and ±5.4 e Å^{-3}.

ment, the fivefold degenerate 3*d* level will split into a lower energy triplet t_{2g} and higher doublet e_g as follows:

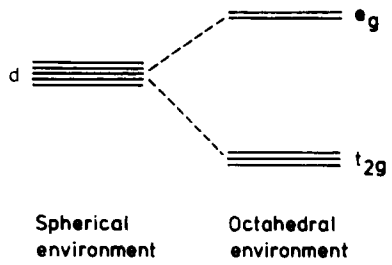

This complex is in a low-spin state and the six 3*d* electrons occupy lower t_{2g} orbitals, leaving the upper e_g orbitals vacant. This electronic structure will give rise to excess electron density in the directions of t_{2g} orbitals, and deficiency in the directions of e_g orbital, compared to a spherically averaged electron-density distribution. The observed deformation density in Fig. 1a agrees well with this expectation based on the simple crystal field model. The theoretical deformation density of $[Co(NO_2)_6]^{3-}$ has been calculated by Ohba using the *ab initio* molecular orbital technique (*55*). Figure 2 shows the theoretical map around the Co atom in the same section as Fig. 1a. Agreement between the experimental and theoretical deformation densities is excellent, except for the peak heights and their positions in the vicinity of the Co atom.

These slight differences are mainly due to the smearing of electron density caused by thermal vibration of the Co atom in crystals. Johansen has also calculated the theoretical deformation density of CoO_6^{10-} by the *ab initio* molecular orbital method (*39*), on the assumption of a regular octahedral geometry with high-spin state $(t_{2g})^5(e_g)^2$. The asphericity of 3*d* electron density is similar to that observed for $[Co(NO_2)_6]^{3-}$.

b. γ-M_2SiO_4. Electron-density distributions around transition metal atoms with different numbers of 3*d* electrons have been studied for three silicate spinels (*49, 50*): γ-Fe_2SiO_4, γ-Co_2SiO_4, and γ-Ni_2SiO_4. They have normal spinel structures, and the transition metal atoms are surrounded by six O^- of an orthosilicate ion forming an octahedron which is slightly distorted trigonally. These silicate crystals are largely ionic, as will be discussed in Section IV,A, and are weak field complexes. The simple crystal field approach discussed above can be applied to these structures. The transition metal ions in octahedral sites, Fe^{2+}, Co^{2+}, and Ni^{2+}, contain different number of 3*d* electrons: six for Fe^{2+}, seven for Co^{2+}, and eight for Ni^{2+}, respectively.

Figure 3 shows the deformation densities around the transition metal ions in these spinels. They are all the same sections containing the transition metal ion and an oxygen atom of the orthosilicate ion. The deformation density around Ni^{2+} (Fig. 3a) is similar to that observed for $[Co(NO_2)_6]^{3-}$. The positive peaks with average height of 1.9 e Å^{-3} appear at 0.46 Å from the Ni nucleus in the direction of threefold axes of the NiO_6 octahedron. They are arranged at the apices of a cube around Ni^{2+}. Unlike $[Co(NO_2)_6]^{3-}$, the exact symmetry around the transition metal sites in these spinels is not O_h but D_{3d}. On lowering the symmetry from O_h to D_{3d}, there remains only one threefold axis out of four of an octahedron. Accordingly, a triply degenerate t_{2g} level further splits into a singlet a_{1g} and a doublet e_g. To avoid confusion, this lower e_g level will be denoted as e_g' hereafter. Energy levels of a_{1g} and e_g' orbitals alternate with each other depending upon whether the MO_6 octahedron is trigonally elongated or compressed. Under the small trigonal distortion and the small extent of mixing between metal 3*d* and ligand orbitals, the electron-density distributions in a_{1g} and e_g' orbitals are nearly identical to that of t_{2g} orbitals in an octahedral environment. Ni^{2+} has eight 3*d* electrons and the electronic configuration is $(a_{1g})^2(e_g')^4(e_g)^2$. This configuration will give rise to deficiency in the e_g orbital and excess in the a_{1g} and e_g' orbitals, the latter two being nearly equal to the t_{2g} orbital of octahedral parentage.

Thus, the observed deformation density around Ni^{2+} is very similar

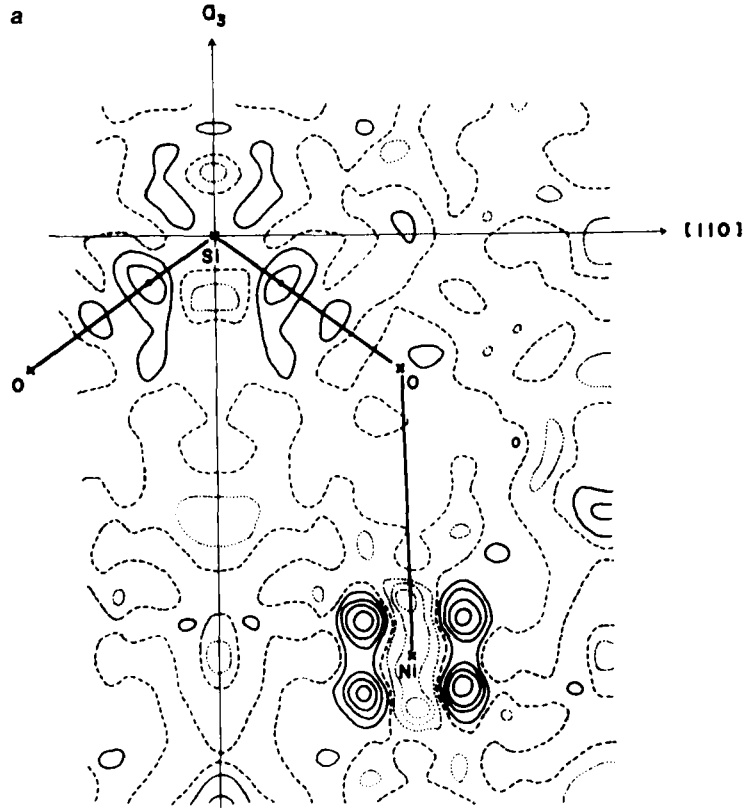

FIG. 3. Deformation densities of γ-M_2SiO_4 in the sections containing C_3 axes and M and O atoms (*49*, *50*). Contours are at intervals of 0.4 e Å^{-3}. (a) γ-Ni_2SiO_4. (b) γ-Co_2SiO_4. (c) γ-Fe_2SiO_4.

to that observed for $[Co(NO_2)_6]^{3-}$. Likewise the observed deformation density around Co^{2+} can be explained. In this case, however, the electronic structure in the weak ligand field may be represented by adding $(a_{1g})^1(e_g')^1$ to the half-occupied $3d$ shell which is spherical. This configuration gives rise to a difference in electron populations in a_{1g} and e_g' orbitals. In fact, the degree of charge accumulation on the threefold axis (a_{1g}) is greater than that on the other pseudo-threefold axes (e_g') in Fig. 3b. Thus the observed difference in charge accumulations may suggest the electronic structure, $(a_{1g})^2(e_g')^3(e_g)^2$ rather than $(a_{1g})^2(e_g')^4(e_g)^1$. γ-Fe_2SiO_4 is a high-spin complex with the electronic structure of a half-occupied $3d$ shell and an electron in the a_{1g} or e_g' orbital. Since the FeO_6^{10-} octahedron is trigonally compressed, a_{1g} is lower in energy than e_g'. Accordingly, the remaining one electron will

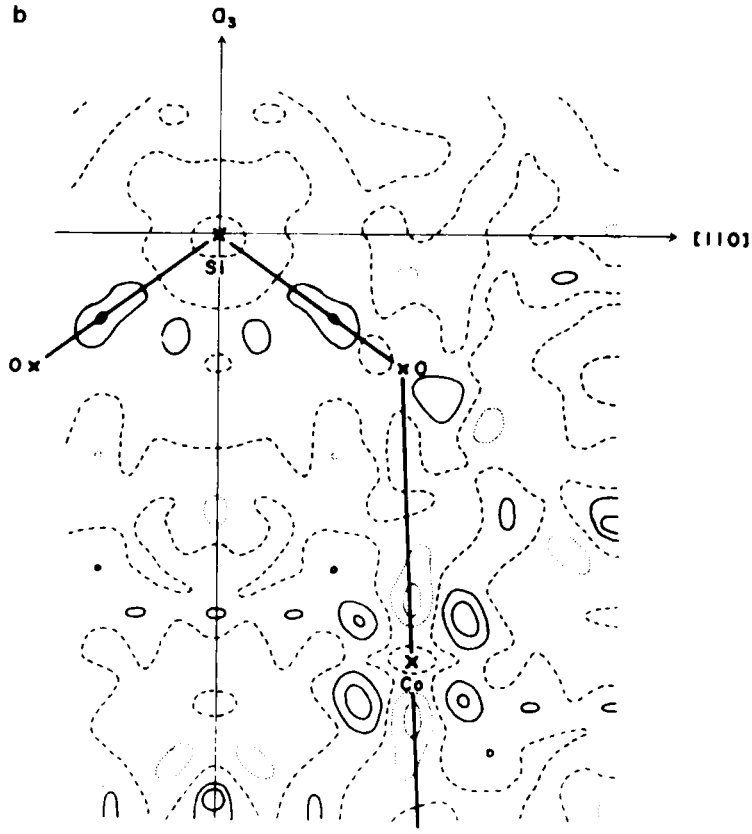

FIG. 3b (see legend p. 38).

occupy the a_{1g} orbital, which has lobes along the threefold axis. The observed deformation density (Fig. 3c) shows only two positive peaks with height of 1.2 e Å^{-3} on the threefold axis at a distance of 0.46 Å from the Fe nucleus. No negative trough appears around Fe^{2+}. This is quite consistent with expectation. Thus the experimental deformation density provides a means of predicting the magnetic properties (*39*) of a transition metal compound.

c. FeS_2. An accurate determination of electron density in iron pyrites, FeS_2, has been made by Stevens *et al.* (*74, 75*). Figure 4 shows the deformation density around the low-spin Fe^{2+} in the trigonally compressed octahedron of six sulfur atoms [Fe—S, 2.2633(2) Å], which differs slightly from that for $[Co(NO_2)_6]^{3-}$. Low-spin ions of Fe^{2+} and Co^{3+} have six 3*d* electrons. The symmetry of the ligand field for the

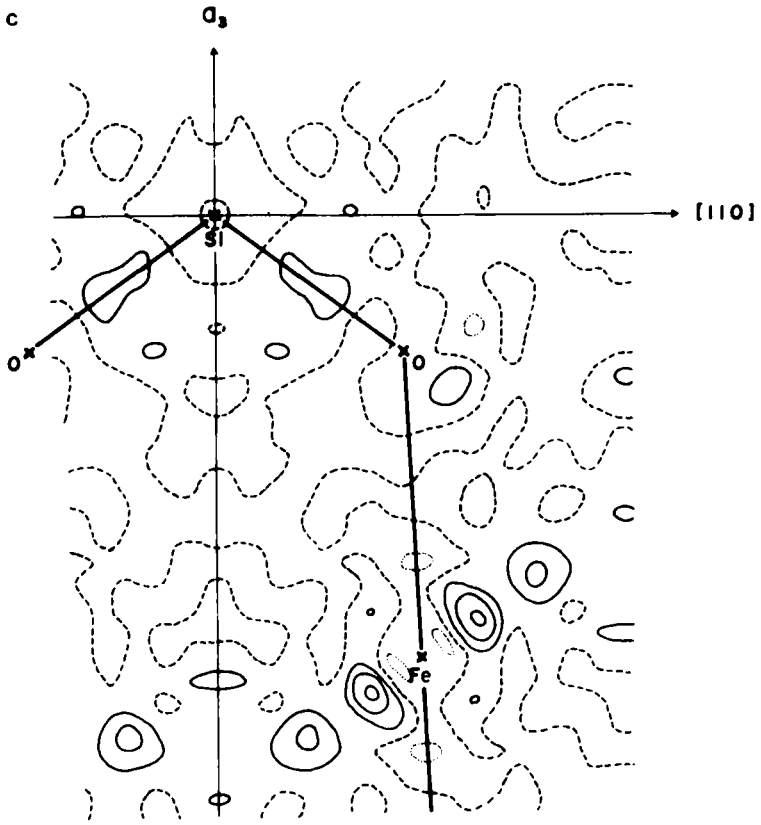

FIG. 3c (see legend p. 38).

Fe^{2+} is not O_h but D_{3d}. This is reflected in the observed deformation density. The peaks on the C_3 axis [1.6(3) e Å^{-3}] are higher than the remaining six on the pseudo-C_3 axis [1.2(2) e Å^{-3}], indicating a preference for occupation of a_{1g} over e_g' orbitals. The former is due to a_{1g} electrons, whereas the latter is due to e_g' electrons. Population analyses of $3d$ electrons were performed in each $3d$-like orbital by using the multipole technique (*75*) (Section IV,C). The analysis yielded reasonable populations for lowest a_{1g}, lower e_g', and upper e_g orbitals: 2.0(1), 3.2(2), and 0.8(2) e, respectively. These populations may be understood in terms of trigonal distortion which raises the energy of the lower e_g' level by mixing with the upper e_g orbital of the same symmetry representation. Another possible explanation for the significant occupation of the upper e_g orbital may be the presence of covalent overlap between

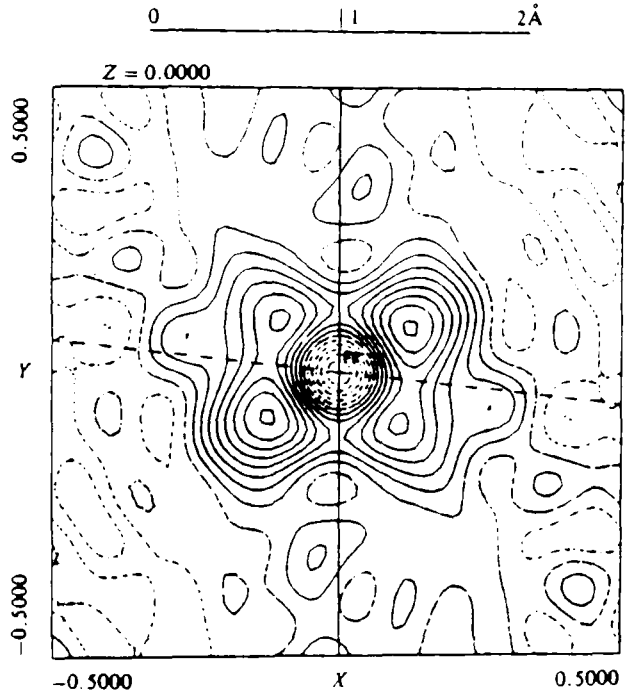

FIG. 4. Deformation density of FeS_2 in a section containing a Fe—S bond and a C_3 axis (75). Contours are at intervals of 0.2 e Å^{-3}. Estimated error of the deformation density is 0.25 e Å^{-3} in a general position.

the metal and ligand atoms. As will be discussed in Section V,B, the upper e_g orbital may be used for bond formation.

d. KMF_3. Tanaka *et al.* have successfully applied the electron population analysis (Section IV,A) to elucidate the electronic structures of transition metal ions in the perovskite-type crystals $KMnF_3$ (*42*), $KCoF_3$ (*41*), $KNiF_3$ (*43*), and $KCuF_3$ (*82*). The transition metal ions are surrounded octahedrally by six F ions, and MF_6^{-} is a regular octahedron except for CuF_6^{4-}. Observed electronic structures are $(t_{2g})^3(e_g)^2$ for MnF_6^{4-}, $(t_{2g})^5(e_g)^2$ for CoF_6^{4-}, and $(t_{2g})^6(e_g)^2$ for NiF_6^{4-}. The results are quite reasonable, indicating a weak field exerted by F ions. The CuF_6^{4-} octahedron is distorted pseudo-tetrahedrally by a cooperative Jahn–Teller effect. Electron population analysis for CuF_6^{4-} was carried out considering the linear combination of 3*d* atomic orbitals.

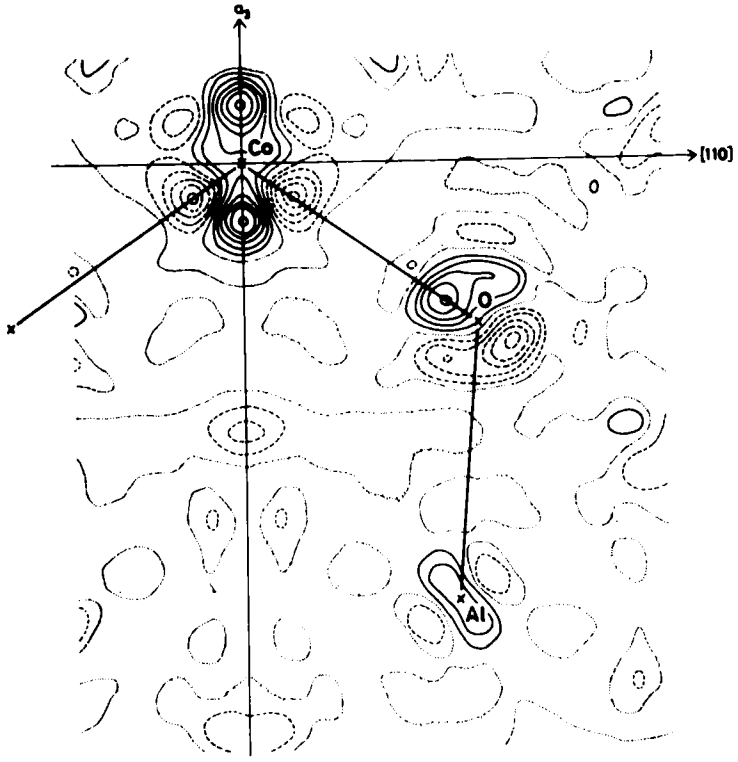

FIG. 5. Deformation density of $CoAl_2O_4$ in the same section as Fig. 2 (*84*). Contours are at intervals of 0.2 e Å^{-3}.

2. *Transition Metal Atoms in Tetrahedral Environments*

Although tetrahedral transition metal complexes are familiar in coordination chemistry, only two tetrahedral complexes have been studied by accurate X-ray crystal structure analysis: CoO_4^{6-} in $CoAl_2O_4$ (*84*) and CrO_4^{2-} in α-K_2CrO_4 (*85*).

a. $CoAl_2O_4$. Figure 5 shows the deformation density in $CoAl_2O_4$ crystals. This compound has a normal spinel structure, and Co^{2+} lies on a tetrahedral site in contrast to the metal ions in the silicate spinels described in the previous section. Co^{2+} is surrounded by four O^{2-} regular tetrahedrally at 1.9457(7) Å. On the deformation density map around Co^{2+}, two sharp positive peaks with a height of 1.3 e Å^{-3} are located at 0.40 Å from the Co nucleus. They are arranged on the three S_4 axes of the CoO_4^{6-} tetrahedron, whereas two large negative (-1.0 e

$Å^{-3}$) and two small negative peaks (-0.6 e $Å^{-3}$) are located in the directions of four C_3 axes at 0.40 Å from the Co nucleus. This arrangement of positive and negative peaks is just opposite to that observed for the transition metal ions in an octahedral environment. A simple crystal field model can also be applied to this case, because of the highly ionic character of this crystal (Section IV,B). In a tetrahedral crystal field, a fivefold degenerate $3d$ level splits into a lower doublet e and a higher triplet t_2 as follows:

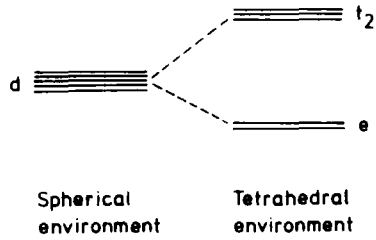

In Co^{2+} ($3d^7$), four $3d$ electrons occupy the lower e orbitals and the remaining three t_2 orbitals. Accordingly, the electronic structure of Co^{2+} in a tetrahedral environment can be described as $(e)^2(t_2)^3 + (e)^2$. This electronic structure displays an aspherical distribution of $3d$ electrons around the Co^{2+}: excess electron density in the direction of e orbitals and deficiency in t_2. The observed deformation density is in good agreement with this expectation. The difference in negative peak heights cannot, however, be accounted for by this simple interpretation. Probably, contributions of $4s$ and $4p$ orbitals of the Co^{2+} ion need be considered. In fact, the net charge of the Co^{2+} is slightly neutralized to $+1.5(1)$, as will be described in Section IV,B.

b. α-K_2CrO_4. Another observed electron-density distribution of a tetrahedral complex, CrO_4^{2-}, is given in Fig. 6. This map shows the average deformation density in the plane containing a Cr atom and two O atoms. CrO_4^{2-} in an α-K_2CrO_4 crystal has an approximately regular tetrahedral structure with the average Cr—O bond distance 1.646(1) Å. On the map of the deformation density around the Cr atom, two significant but weak positive peaks with a height of 0.20(4) e $Å^{-3}$ appear at 0.40 Å from the Cr nucleus on the extension of the O—Cr bonds. Two negative peaks [$-0.30(4)$ e $Å^{-3}$] also lie at 0.35 Å from the Cr nucleus on the Cr—O bonds. In addition, there is a large positive region at the center of the Cr—O bond, which can be attributed to the charge accumulation due to the Cr—O multiple bond. The peak-top position of this broad positive region is located at 0.97 and 0.68 Å from

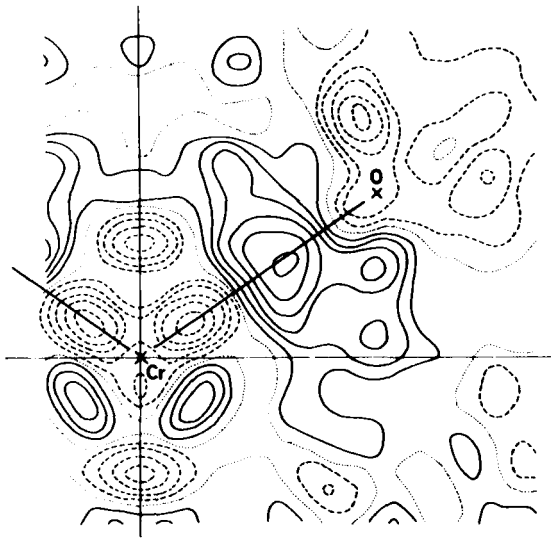

FIG. 6. Averaged deformation density of α-K_2CrO_4 in the plane containing a Cr and two O atoms (*85*). Contours are at intervals of 0.05 e Å^{-3}. Estimated error of the deformation density is 0.04 e Å^{-3} at a general position.

the Cr and O atoms, respectively. Negative troughs appear on the S_4 axis of tetrahedron at 0.67 Å from the Cr nucleus. On this deformation map, residual peaks distant from the O atoms are meaningless, because this map was obtained by averaging all the deformation densities on the chemically equivalent planes in which dispositions of K^+ around the CrO_4^{2-} are different.

The central Cr atom of this oxo anion takes a high formal oxidation number of +6, and has no 3*d* electrons. If CrO_4^{2-} had a purely ionic structure, the electron-density distribution around a Cr^{6+} ion would be spherically symmetrical like that in TiO_2 (*68*). In fact, the deformation density around Ti^{4+} surrounded octahedrally by six O^{2-} shows no significant peaks. Direct integration of the electron density around each atom in a α-K_2CrO_4 crystal gives the net charge of the Cr atom as the largely neutralized value of +0.1 (Section IV,B). This net charge may be somewhat overestimated, because of the coarse estimation for each atomic region. However, it is certain that the net charge of the Cr atom is much lower than the formal oxidation number. This fact suggests that 3*d* atomic orbitals as well as 4*s* and 4*p* of the Cr atom largely contribute to the Cr—O bonding orbitals and they are occupied by the electrons donated from O atoms. As seen from the short Cr—O distance, the Cr atomic orbitals considerably overlap the O

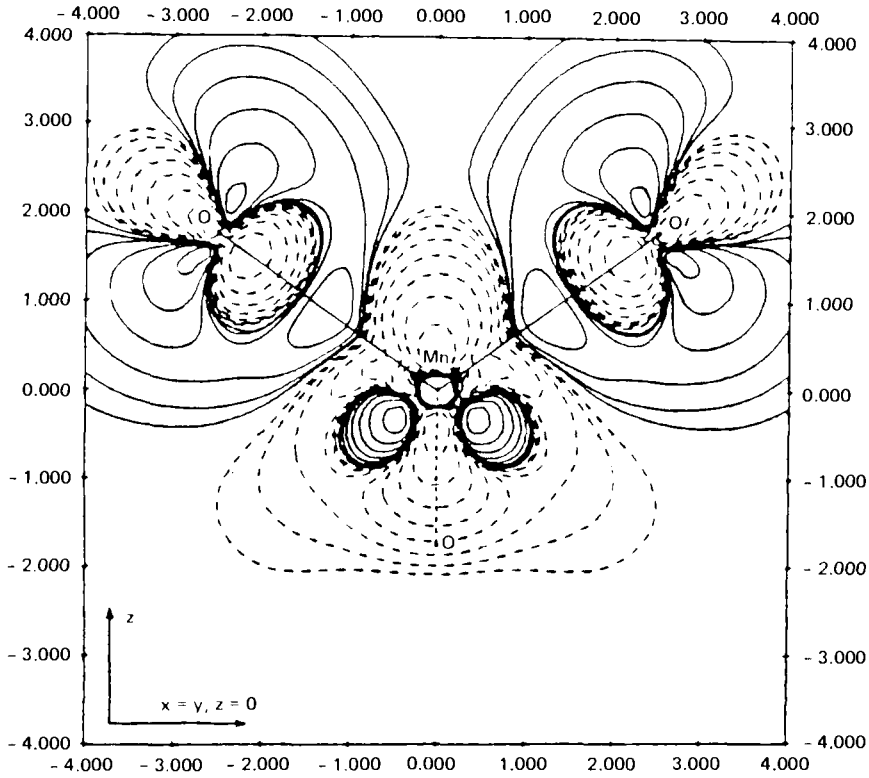

FIG. 7. Theoretical deformation density of MnO_4^- in the same plane as Fig. 6 (*39*). First contours are 0.017 *e* Å $^{-3}$, respectively, and neighboring contours differ by a factor 2.

atomic orbitals (Section V,C). Consequently, the deformation density of CrO_4^{2-} cannot be accounted for by a simple crystal field model. Johansen has calculated the theoretical deformation density for the isoelectronic ion of MnO_4^- by the *ab initio* Hartree–Fock configuration interaction technique (*39*).

It is reasonable to compare the observed deformation density of CrO_4^{2-} with the theoretical one for MnO_4^-, since the electronic structures of both systems can be regarded as identical except for the different oxidation numbers of the central transition metal atoms. Figure 7 shows the theoretical deformation density around the Mn nucleus on the same section as Fig. 6. Aspherical electron-density distributions around the metal atoms closely resemble each other. The theoretical deformation density presents pronounced positive peaks around the Mn nucleus at 0.30 Å with peak height of 2 *e* Å^{-3} on the extension of the O—Mn bonds. Positive peak height and the distribution of nega-

tive regions differ slightly from the observed ones; however, the charge migration upon bond formation may be well reproduced by the molecular orbital calculation. Considering the 3*d* atomic orbitals of the transition metal atom in the tetrahedral MO_4^{n-}, they split into *e* and t_2 orbitals as in the CoO_4^{6-} system described above. These t_2 and *e* orbitals contribute to σ- and π-bonding orbitals of the Cr—O bond, respectively. Johansen claims that charge accumulation on the extension of the O—Mn bond arises from the excess charge density in the t_2 orbital and the deficiency in the *e* orbital. A similar result has been reported by Johnson and Smith (*40*), who calculated the electron-density distribution in MnO_4^- by the SCF-Xα-SW method.

B. Transition Metal Complexes Having Short Metal–Metal Bonds

An unusually short metal–metal bond in a transition metal complex was first observed in the crystal structure analysis of $K_2[Re_2Cl_8] \cdot 2H_2O$ by Cotton and Harris (*25*). Much attention has been given to the short metal–metal bond, and extensive magnetic and spectroscopic studies have been carried out on these complexes. Accurate determinations of electron-density distributions in crystals of $Cr_2(CH_3CO_2)_4 \cdot 2H_2O$ (*10*) and $Mo_2(CH_3CO_2)_4$ (*33*) have been carried out by single crystal X-ray diffraction; for these compounds very short Cr—Cr and Mo—Mo bonds were reported (*23, 24, 86*). These metal–metal bonds are considered to be quadruple bonds of the $\sigma^2\pi^4\delta^2$ type. The observed deformation density of $Mo_2(CH_3CO_2)_4$ shows the diffuse positive peak at the center of the metal–metal bond which can be attributed to the charge accumulation due to the direct metal–metal bonding. No positive peak has, however, been observed for $Cr_2(CH_3CO_2)_4 \cdot 2H_2O$. The difference in the deformation densities is due to the different natures of the metal–metal bonds.

a. *$Mo_2(CH_3CO_2)_4$*. The molecular structure of $Mo_2(CH_3CO_2)_4$ is presented in Fig. 8. Two Mo atoms are bridged by four acetyl groups and form a dimeric structure. The Mo—Mo distance of 2.0885(5) Å is remarkably shorter than the interatomic distance in metallic crystal (2.725 Å) (*36*). Each Mo^{2+} ion is surrounded by four O atoms of acetyl groups with the average distance of 2.118(2) Å in a square planar array. The geometry of the complex can be approximated as D_{4h}.

Figure 9 shows the deformation densities in crystals of $Mo_2(CH_3CO_2)_4$. They show the remarkable feature at the center of the Mo—Mo bond with a diffuse but definite positive region with a height of 0.2 *e* Å^{-3}. This positive region extends perpendicularly to the

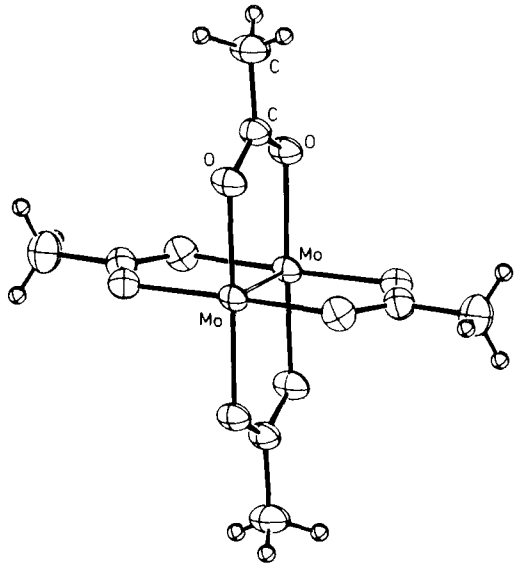

FIG. 8. Molecular structure of $Mo_2(CH_3CO_2)_4$.

Mo—Mo axis. Positive peaks are also located on the extension of the Mo—Mo bond at 0.42 Å from the Mo nuclei (Fig. 9a). Figure 9b shows two positive peaks in the vicinities of the Mo nuclei in the directions bisecting the O—Mo—O bond angles, which are, in all, arranged at the four corners of the square around each Mo nucleus. The deformation density in the vicinity of each Mo atom is quite reasonable when the square planar arrangement of four O atoms (D_{4h}) around the Mo^{2+} ($4d^4$) is assumed. In D_{4h} ligand field, both the t_{2g} and e_g levels in the O_h field further split into two levels. Although the energy levels of these d orbitals alternate with each other depending upon an axial ligand field, the energy diagram of the square planar environment may be represented as follows:

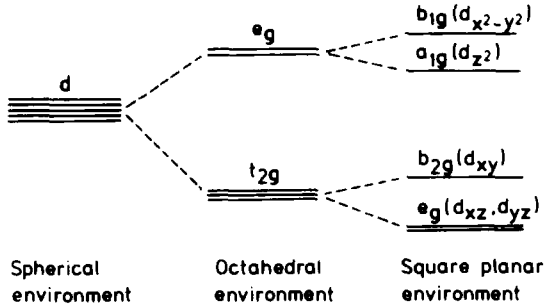

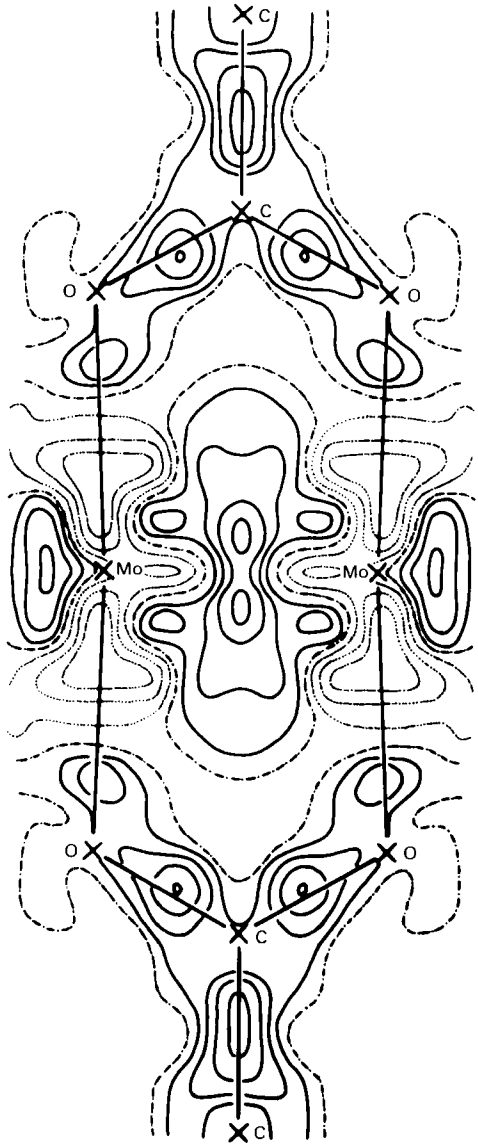

FIG. 9. Deformation density of $Mo_2(CH_3CO_2)_4$ (*33*). Contours are at intervals of 0.1 *e* $Å^{-3}$. (a) A section through the Mo—Mo bond and two acetyl groups. (b) A section through the Mo—Mo bond and bisecting the two planes of the adjacent acetyl groups.

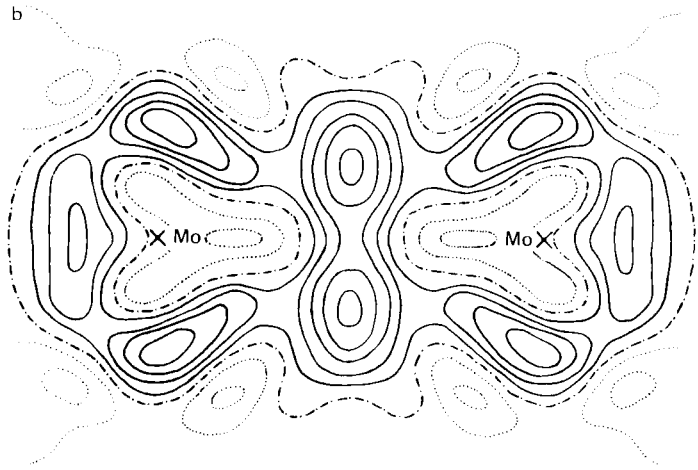

FIG. 9b (see legend p. 48).

Four $4d$ electrons of the Mo^{2+} will occupy the lower four orbitals, leaving the highest b_{1g} ($d_{x^2-y^2}$) vacant. This electronic structure will give rise to deficient electron density in the direction of the Mo—O axis, being consistent with the observed deformation density.

When we try to describe the charge accumulation at the center of the Mo—Mo bond, a molecular orbital theory should be applied to the dimeric structure in place of a simple crystal field model. Cotton proposed a metal–metal quadruple bond for the Re—Re bond in $K_2[Re_2Cl_8] \cdot 2H_2O$ (*25*), in which $Re_2Cl_8^{2-}$ has the same structure as the Mo_2O_8 cluster, in order to explain the unusually short Re—Re distance (2.24 Å) and the eclipsed form of the two Cl_4 squares bonded to Re atoms. We can use the same molecular orbital scheme for the Mo_2O_8 cluster. Following the energy diagram of square planar complexes, we may assume that four d orbitals except for the strongly antibonding $d_{x^2-y^2}$ orbital are available for interaction with the neighboring Mo atom. Viewed along the metal–metal axis, the d_{z^2} orbital has σ symmetry, the d_{xz} and d_{yz} have π symmetry, and the d_{xy} has δ symmetry, respectively. If the two O_4 squares are eclipsed, the d_{xy} orbital on each metal atom will overlap and give a bonding orbital, but if the squares are staggered the overlap will be zero. Thus the orbitals involved in the bond are the four d orbitals: the d_{z^2} orbital (σ bonding orbital) overlap strongly, d_{xz} and d_{yz} (π bonding orbitals) less so, and d_{xy} (δ bonding orbital) weakest of all. Since each Mo^{2+} ion has four $4d$ electrons, eight $4d$ electrons of both ions fill the σ, two π, and the δ metal–metal bonding orbitals, giving four filled bonding orbitals or a quadruple

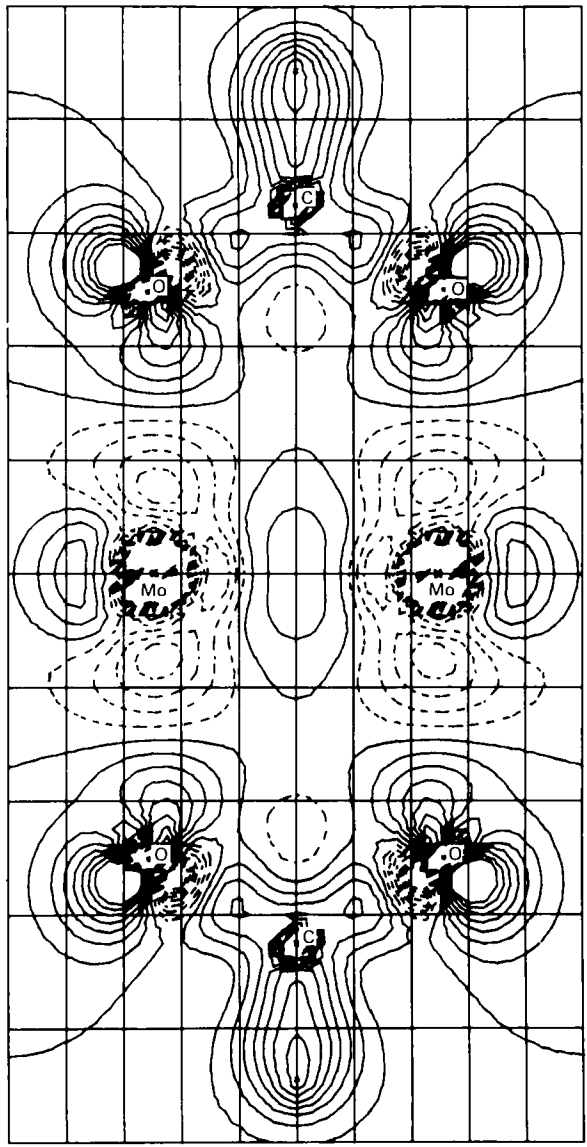

FIG. 10. Theoretical deformation density of $Mo_2(HCO)_4$ in the same plane as Fig. 9a (*33*). Contours are at intervals of 0.1 e Å $^{-3}$.

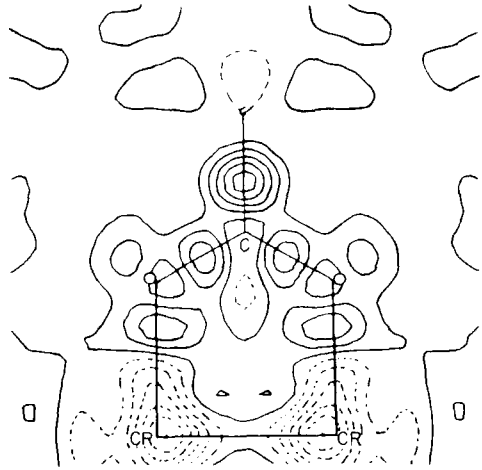

FIG. 11. Averaged deformation density of $Cr_2(CH_3CO_2)_4 \cdot 2H_2O$ in the plane through the Cr—Cr bond and two acetyl and two water groups (*10*). Contours are at intervals of 0.1 *e* Å $^{-3}$.

metal–metal bond of $\sigma^2\pi^4\delta^2$ type. Following the molecular orbital theory described above, the positive peak at the center of the Mo—Mo bond (Fig. 9) may be attributed to the charge accumulation due to the Mo—Mo quadruple bond. The positive region extends perpendicularly to the Mo—Mo axis, being consistent with the π bond nature of the Mo—Mo bond. No distinct feature of the δ bond can, however, be observed on the deformation density. It may be due to the weak and diffuse overlap between the d_{xy} orbitals. Bénard has calculated the theoretical deformation density of $Mo_2(HCO_2)_4$ by the *ab initio* configuration interaction MO method (*33*). Figure 10 shows the theoretical deformation density, which compares well with the observed one. In particular, a diffuse metal–metal bonding peak is well reproduced by the molecular orbital calculation.

b. $Cr_2(CH_3CO_2)_4 \cdot 2H_2O$. $Cr_2(CH_3CO_2)_4 \cdot 2H_2O$ has the same structure as $Mo_2(CH_3CO_2)_4$ except for the axial water molecules. Each Cr^{2+} has four $3d$ electrons, and following a classical molecular orbital scheme described above, the Cr—Cr bond can also be described as a metal–metal quadruple bond of $\sigma^2\pi^4\delta^2$ type. The Cr—Cr distance of 2.3532(4) Å is significantly longer than the Mo—Mo distance [2.0885(5) Å], suggesting a weaker metal–metal interaction than the Mo–Mo bond. Figure 11 shows the deformation density in crystals of $Cr_2(CH_3CO_2)_4 \cdot 2H_2O$ (*10*). There are no positive peaks on the Cr—Cr

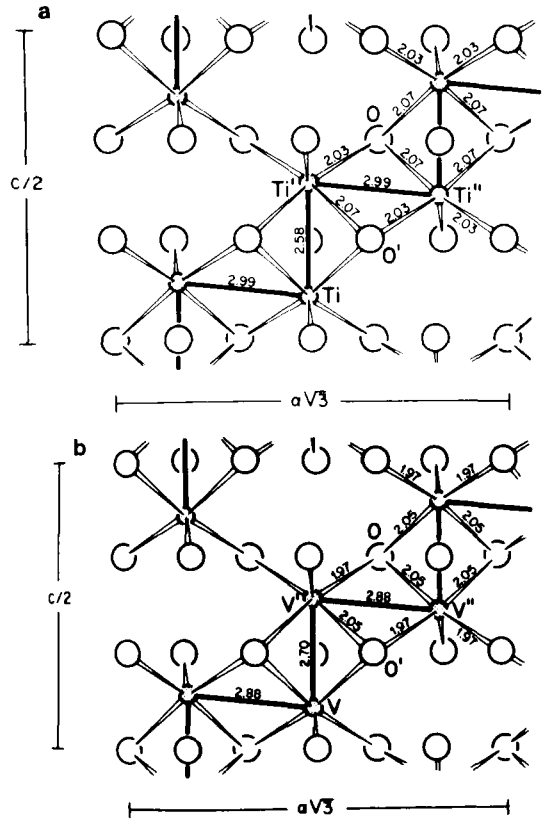

FIG. 12. Projections of the crystal structures on the $(11\bar{2}0)$ plane (*87*, *88*). (a) Ti_2O_3. (b) V_2O_3.

axis or in the vicinities of Cr atoms. These features are largely different from those observed in $Mo_2(CH_3CO_2)_4$. Bénard has calculated the theoretical deformation density of the model complex of $Cr_2(HCO_2)_4$ by the *ab initio* CI MO method (*9*). This model structure is different with respect to the axial water coordinations. The theoretical deformation density shows no positive peaks at the center of the Cr—Cr bond, in agreement with the observed deformation density. Bénard claimed that an *ab initio* molecular orbital calculation for the $Cr_2(HCO_2)_4$ system including the configuration interactions gave a large contribution of dissociative configuration, $\sigma^2\delta^2\delta^{*2}\sigma^{*2}$, for the Cr—Cr bond, and the weight of the strongly bonded $\sigma^2\pi^4\delta^2$ configuration was only 18% at equilibrium. Thus the strength of the Cr—Cr bond is annihilated by the large contribution of antibonding configurations, and the Cr—Cr bond order becomes less than the formal value of 4, being consistent

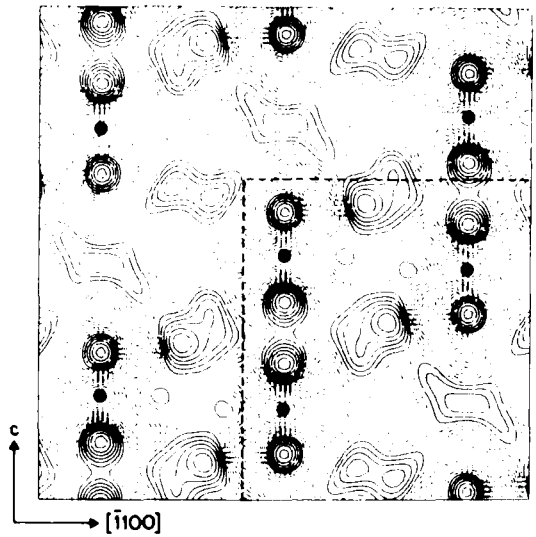

FIG. 13. Deformation density of Ti_2O_3 in the $(11\bar{2}0)$ section (*88*). Filled circles indicate the Ti positions. Contours are at intervals of 0.02 e Å^{-3}.

with the longer Cr—Cr bond distance. The deformation density around the Cr—Cr bond can be interpreted by the above explanation, which takes into account the radial distributions of $3d$ and $4d$ orbitals, $3d$ orbitals of a Cr atom being less expanded than the $4d$ orbitals of a Mo atom, and giving less overlap and hence a weak bond. Axial water molecules may also affect the Cr—Cr bond.

c. Ti_2O_3 and V_2O_3. The transition metal oxides Ti_2O_3 and V_2O_3 are both isostructural with corundum (α-Al_2O_3), but their electrical properties are distinctly different: Ti_2O_3 is an insulator at room temperature, whereas V_2O_3 is metallic. These electrical properties are expected to be closely related to the directions of metal–metal interactions; metal–metal bonds are formed along the c axis in the Ti_2O_3 crystal and they are perpendicular to the c axis in the V_2O_3 crystal. Observed deformation densities of both crystals clearly display the difference in the metal–metal bond directions (*87, 88*). The atomic arrangements in both crystals with their interatomic distances are depicted in Fig. 12a and b, respectively. In these crystals, the metal ions sit on a crystallographic threefold axis, and are surrounded octahedrally by six O^{2-}. In addition, four metal ions are located in a second neighboring region: three of the four are arranged on an approximate plane perpendicular to the C_3 axis and the remaining one lies on one side of the C_3 axis. Figure 13 shows the deformation density in crystals

of Ti_2O_3 in the same section as Fig. 12. Two significant positive peaks appear on both sides of the C_3 axis at 0.8 Å from the Ti nucleus. Each positive peak between the closest contact pair of Ti atoms is fused together, indicating some direct interaction, a metal–metal single bond, between the Ti atoms. On the other hand, no positive peak is observed on a plane perpendicular to the C_3 axis. The deformation density seems to display the direct metal–metal interactions on directions not perpendicular to but along the threefold axes.

Figure 14a and b shows the deformation densities in crystals of V_2O_3 in the same plane as Fig. 12 and in a plane perpendicular to the C_3 axis, respectively. Three positive peaks appear in the vicinities of V atoms in the plane perpendicular to the C_3 axis, whereas no peak is observed along the C_3 axis. The positive peaks are elongated and fused with the positive peak in the vicinity of the neighboring V atom. The deformation density also seems to display direct metal–metal interactions between the V atoms in the directions perpendicular to the threefold axes. A two-dimensional layer structure in V_2O_3 crystals is formed by these metal–metal interactions. In this way the electrical properties of Ti_2O_3 and V_2O_3 crystals are well interpreted by the direct metal–metal bonds revealed by the observed deformation densities. Unfortunately, however, the deformation density available at present gives little information about the strength of a metal–metal interaction, in other words, conductivity.

Aspherical distributions around the metal ions can be described by a simple crystal field model. Ti^{3+} and V^{3+} have one and two $3d$ electrons, respectively. If the atoms distant from the second neighboring region are disregarded for simplicity, environments around the metal ions can be taken as trigonally distorted octahedra (D_{3d}). Following the energy diagram of $3d$ atomic orbitals, the one $3d$ electron of Ti^{3+} occupies the a_{1g} orbital whereas the two of V^{3+} occupy the lower e_g' orbital. The difference in electronic structures can be interpreted by the trigonal distortions of both MO_6 octahedra. The average angles between the C_3 axes and M—O bonds are 56.3° for TiO_6 and 54.4° for VO_6 octahedra (54.7° for a regular octahedron).

C. Organometallic Compounds

Organometallic compounds commonly exhibit high reactivities compared to the coordination compounds described previously. Their visible and/or ultraviolet absorption spectra are so complicated that the assignments are often difficult. Theoretical calculations, their reactivities, and spectroscopic data suggest the characteristic natures of chem-

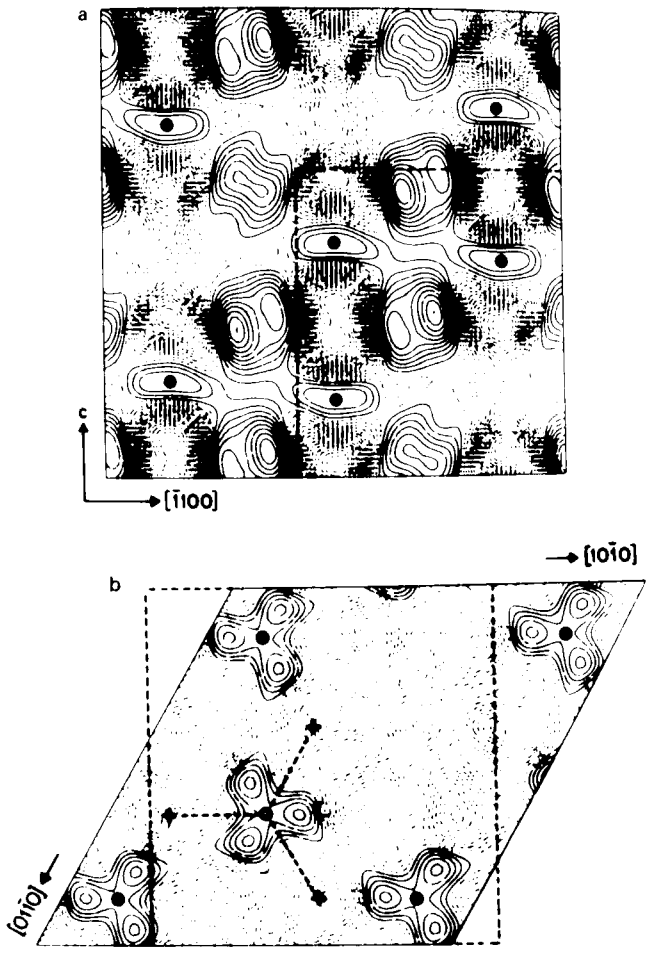

FIG. 14. Deformation density of V_2O_3 in (a) the (11$\bar{2}$0) section and (b) the section perpendicular to C_3 axis (c axis) bisecting the V′—V″ (2.88 Å) bond (*87*). Filled circles indicate the V positions and crosses the O atoms. Contours are at intervals of 0.02 *e* Å $^{-3}$.

ical bond involved, such as a highly covalent and diffuse character of the bond. Accurate X-ray diffraction studies have been made for some organometallic compounds in order to reveal the nature of the chemical bonds. Electron-density distributions in the crystals have been observed for organometallic compounds containing carbonyl and cyclopentadienyl molecules. Unfortunately, the observed deformation densities do not give clear pictures of the bonds, because of the lack of a remarkable charge accumulation upon bond formation and insufficient

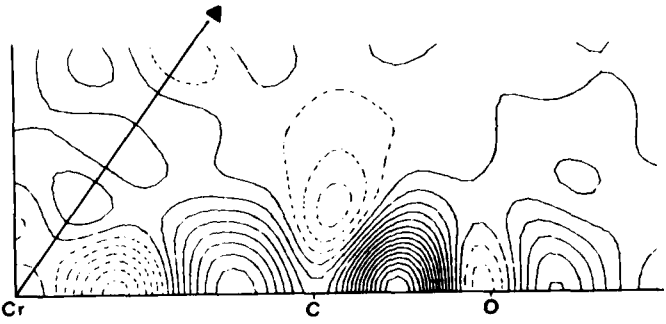

FIG. 15. Averaged deformation density of $Cr(CO)_6$ in the plane containing one Cr—C—O bond and bisecting two other bonds (*63*). Contours are at intervals of 0.05 *e* $Å^{-3}$. Estimated error of the deformation density is 0.03 *e* $Å^{-3}$ at a general position.

accuracy of the observed deformation density. On the other hand, aspherical distributions of 3*d* electrons have been clearly detected in the vicinities of transition metal nuclei.

a. Cr(CO)₆. The accurate electron-density distribution in crystals of the simple organometallic compound, chromium hexacarbonyl, $Cr(CO)_6$, has been determined by Rees and Mitschler (*61, 63*). This diamagnetic complex has a regular octahedral structure with O_h symmetry and the average Cr—C and C—O distances are 1.914(2) and 1.140(1) Å, respectively. Figure 15 shows the observed deformation density in the plane containing one Cr—C—O bond and bisecting two other bonds. The deformation map has been obtained by averaging the deformation densities in the crystallographically independent but chemically equivalent planes (*61*). On the map, a significant aspherical distribution appears around the Cr nucleus. A weak positive peak with height of 0.10(3) *e* $Å^{-3}$ is located on the threefold axis of a CrC_6 octahedron at about 0.75 Å from the Cr nucleus, and a negative trough of -0.30 *e* $Å^{-3}$ on the fourfold axis at 0.65 Å. The arrangement of positive and negative peaks around the Cr nucleus may be compared with that of $[Co(NO_2)_6]^{3-}$ (Fig. 1), exhibiting excess electron density in the t_{2g} orbital and deficiency in the e_g. Remarkable differences, however, exist in the positive and negative peak heights and their positions from the metal nucleus. The peaks around the Cr atom are very weak and far from the nucleus compared to those around the Co nucleus (Section III,A,1). They are not due to the thermal smearing of electron densities, because the thermal vibrations of both atoms are of the same order of magnitudes: root mean square amplitudes of Cr atom in $Cr(CO)_6$ and Co in $K_2Na[Co(NO_2)_6]$ crystals are 0.08 (74 K) and 0.10

Å (298 K), respectively. Consequently, the weak asphericity observed in the deformation density may be genuine and suggest a small difference of $3d$ electron occupancies in t_{2g} and e_g orbitals.

Rees and Mitschler have estimated the $3d$ electron populations in t_{2g} and e_g orbitals for both limited electronic configurations of $(3d)^5(4s)^1$ and $(3d)^6$ (*63*). The electron population in the $4s$ orbital was not refined because a diffuse distribution of $4s$ electrons affects only a small number of structure amplitudes with very low reflection angles. The estimated electronic configurations of a Cr atom are $3d(t_{2g})^{3.8}3d(e_g)^{1.2}(4s)^1$ and $3d(t_{2g})^{4.5}3d(e_g)^{1.5}$, respectively, being consistent with the weak asphericity in $3d$ electron distribution.

A number of molecular orbital calculations (*2, 32*) have been performed on this system to investigate its electronic structure and bonding nature. Despite the considerable disagreement between the corresponding results, such as the metal charge and the orbital populations of chromium $3d$ orbitals, the diffuse and bonding characters of the $3d$ orbitals have been clearly revealed by the theoretical calculations, in contrast to the contracted and nonbonding characters of metal $3d$ orbitals in the transition metal complexes. Both the t_{2g} and e_g orbitals as well as $4s$ and $4p$ orbitals are significantly overlapped by the σ and π orbitals of carbonyl groups and form σ and π bonding orbitals, respectively. In $Cr(CO)_6$, the originally empty $3d(e_g)$ orbitals receive significant amounts of electrons from σ orbitals of carbonyl groups, while the completely filled $3d(t_{2g})$ orbitals give electrons to the π orbitals. The difference in the $3d$ electron populations between t_{2g} and e_g orbitals decreases in this way, giving rise to the small asphericity in the observed deformation density around the Cr nucleus. Theoretical calculations also revealed an equal amount of σ donation and π-back donation. The estimated net charge of Cr atom [$+0.2(1)$ e] (Section IV,B) agrees with these calculations. A feature of this π-back donation clearly appears in the observed deformation density. The positive peak located on the Cr—C bond axis, which can be attributed to the charge accumulation upon the Cr—C bond formation, is spread out perpendicularly to the bond axis and fused with the positive peak in the direction of the t_{2g} orbital.

b. $[(C_5H_5)Fe(CO)_2]_2$. Organometallic compounds containing π-cyclopentadienyl groups are very attractive for the investigation of the chemical bond formed by the transition metal atom and π-cyclic group. Electron-density distribution in the $[(C_5H_5)Fe(CO)_2]_2$ crystal has been observed (*52*), in which the π-cyclopentadienyl group is coordinated to an Fe atom. The molecular structure of this compound is depicted in

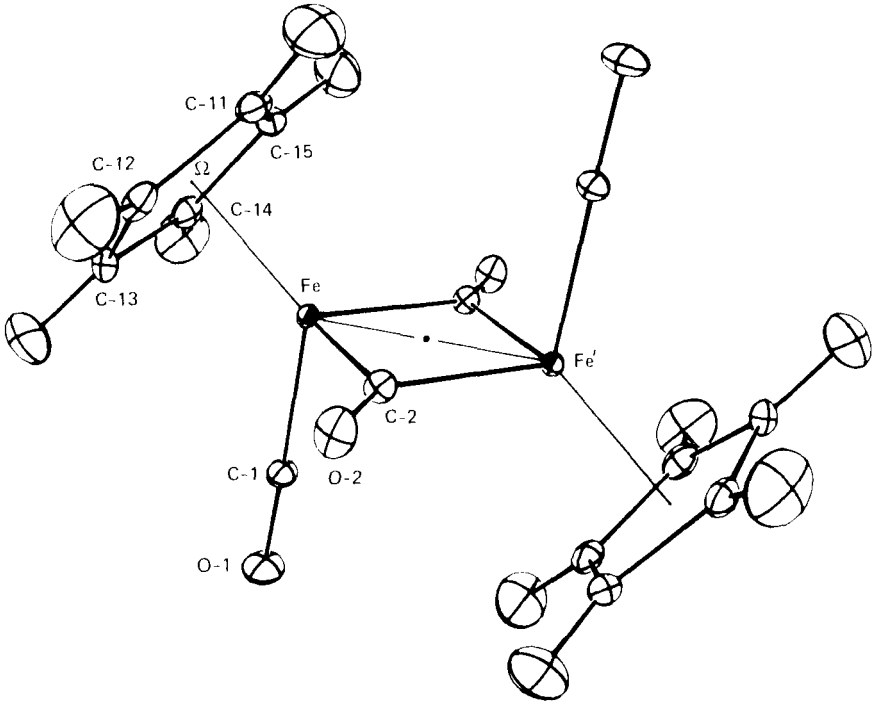

FIG. 16. Molecular structure of $[(C_5H_5)Fe(CO)_2]_2$ (*52*).

Fig. 16; it is approximately characterized by a symmetry group C_{2h}. Some important bond distances and angles are tabulated in Table II. Two Fe atoms are bridged by two carbonyl groups, a short Fe—Fe separation being 2.539(1) Å [2.474 Å in metallic iron (*56*)]. This binuclear complex is diamagnetic, for which a direct metal–metal bond is required for the spin coupling mechanism between the two Fe atoms in analogy with a diamagnetic compound, $[(C_6H_5)_2PCo(C_5H_5)]_2$ (*12*). The π-cyclopentadienyl group has an almost regular pentagonal geometry with the C—C bond lengths ranging from 1.411(1) to 1.435(1) Å, and 6 π-electrons. Consequently, the Fe atom takes a formal oxidation number of +1, and has seven $3d$ electrons. The Fe—C distances to the cyclopentadienyl ring are in the range 2.104(1)–2.146(1) Å, which are slightly longer than those in ferrocene (*11*).

Observed deformation densities are shown in Fig. 17a–d. The aspherical distribution of $3d$ electrons can be clearly seen in the vicinity of the Fe nucleus. Two positive peaks with 0.5 e Å^{-3} are located at

TABLE II

SELECTED BOND DISTANCES (Å) AND ANGLES (°) WITHIN THE $[(C_5H_5)Fe(CO)_2]_2$ COMPLEX GIVEN BY NEUTRON DIFFRACTION MEASUREMENT[a]

Fe—Fe'[b]	2.5390(6)	C-1—O-1	1.1498(8)
Fe—C-1	1.7626(6)	C-2—O-2	1.1782(7)
Fe—C-2	1.9280(5)	C-11—C-12	1.4231(8)
Fe—C-2'	1.9210(6)	C-12—C-13	1.4165(8)
Fe—C-11	2.1392(6)	C-13—C-14	1.4351(8)
Fe—C-12	2.1360(6)	C-14—C-15	1.4106(8)
Fe—C-13	2.1036(6)	C-15—C-11	1.4249(8)
Fe—C-14	2.1173(6)		
Fe—C-15	2.1456(6)		
Fe—Ω	1.7512		
C-2—Fe—C-2'	97.45(2)	C-1—Fe—C-2'	94.61(3)
C-1—Fe—C-2	92.95(3)	C-1—Fe—Fe'	95.73(2)

[a] From Ref. (*52*).

[b] Prime denotes the atom transformed by a center of symmetry which lies on the center of the Fe—Fe bond.

about 0.6 Å from the Fe nucleus on both sides of it on a line passing through the Fe nucleus and the center of the cyclopentadienyl moiety. A positive region with cylindrical shape also appears around the Fe nucleus in the plane perpendicular to the line. Taking into account the environment around the Fe atom, five degenerate $3d$ atomic orbitals of the Fe atom split into lower energy nonbonding d_{z^2}, $d_{x^2-y^2}$, and d_{xy} orbitals and higher antibonding d_{xz} and d_{yz} orbitals (the z axis is taken perpendicular to the cyclopentadienyl ring, the y axis perpendicular to the molecular plane containing a Fe—Fe bond and two nonbridged CO groups). Six $3d$ electrons among the seven of the Fe atom will formally occupy the lower nonbonding d_{z^2}, $d_{x^2-y^2}$, and d_{xy} orbitals and the antibonding d_{xz} and d_{yz} orbitals are left vacant. The remaining one $3d$ electron will be available for the Fe—Fe single bond.

The electronic structure will give rise to excess electron density in the directions of three nonbonding orbitals and deficiency in the directions of two antibonding orbitals. This simple expectation reasonably reproduces the observed asphericity of $3d$ electron distribution in the vicinity of the Fe atom. The magnitude of its asphericity is, however, small as in $Cr(CO)_6$, in contrast to that in $[Co(NO_2)_6]^{3-}$ (Fig. 1). Likewise the $3d$ orbitals in $Cr(CO)_6$, antibonding d_{xz} and d_{yz} orbitals, will

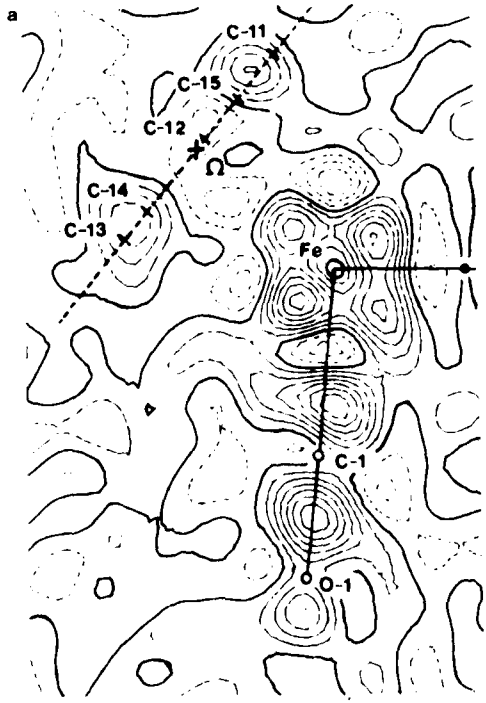

FIG. 17. Deformation density of $[(C_5H_5)Fe(CO)_2]_2$ (*52*). Contours are at intervals of 0.1 e Å^{-3}. (a) A section containing the Fe—Fe bond and the terminal CO group. (b) A section perpendicular to (a) and containing the Fe—C—O bond. (c) A section containing the Fe—Fe bond and the bridged CO group. (d) A section parallel to the cyclopentadienyl ring and through a Fe atom.

appreciably contribute to the σ bonding orbitals, and nonbonding orbitals to the π-back bonding orbitals. *Ab initio* (*9b*) and semiempirical molecular orbital calculations (*52*) have been carried out for this system. The theoretical calculations gave the significant populations of about one $3d$ electron for each initially vacant d_{xz} and d_{yz} orbital and a decrease in the nonbonding orbitals. The observed deformation density in the vicinity of the Fe nucleus agrees well with the theoretical one.

In the deformation density in Fig. 17c, no charge accumulation is observed at the center of the Fe—Fe single bond. The lack of significant feature in the deformation density may be related to the small bond overlap population between the two Fe atoms given by the theoretical calculations. In view of the diffuse manner of charge accumulation upon a metal–metal bond formation as described in the Cr—Cr and Mo—Mo quadruple bonds (Section III,B), it cannot be decided

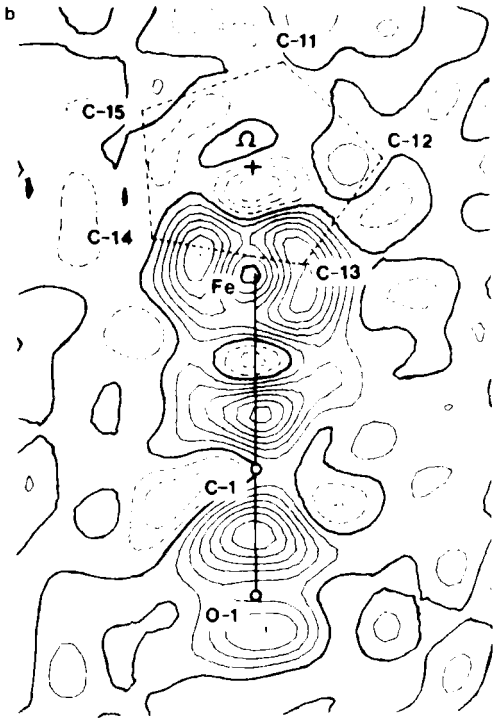

FIG. 17b (see legend p. 60).

whether a Fe—Fe single bond is strong or not from this deformation density.

c. $(C_6H_6)Cr(CO)_3$ *and* $(\eta^5\text{-}C_5H_5Ni)_2C_2H_2$. Accurate measurements have been carried out at liquid nitrogen temperature for $(C_6H_6)Cr(CO)_3$ (*62*) and $(\eta^5\text{-}C_5H_5Ni)_2C_2H_2$ (*90*), and aspherical distributions have been revealed in the vicinities of metal atoms. However, these observed deformation densities exhibit mysterious distributions of positive and negative peaks around the metal nuclei, and could not be accounted for either by simple crystal field models or theoretical calculations (*9b*).

The molecular structure of $(C_6H_6)Cr(CO)_3$ is characterized by a C_{3v} symmetry, in which a Cr atom is coordinated by a benzene molecule and three carbonyl groups. The average Cr—C(benzene) and Cr—C(CO) distances are 2.230(7) and 1.842(4) Å, respectively. The benzene ring is slightly distorted and its symmetry is C_{3v} instead of the higher D_{6h}. The average value of three C—C distances trans to CO

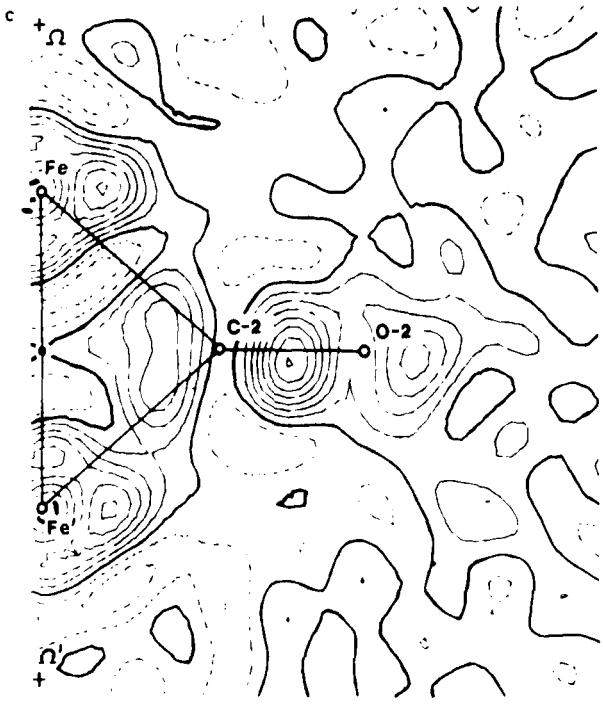

FIG. 17c (see legend p. 60).

groups [1.404(3) Å] is significantly shorter than that of the remaining three distances [1.420(3) Å]. The observed deformation density shows two positive peaks with height of 1.5 e Å^{-3} in the vicinity of the Cr nucleus. They are located in the direction roughly parallel to but largely different from the threefold axis of the complex. This feature does not correspond to the C_{3v} environment around the Cr atom, and cannot be explained by a molecular orbital theory. Since the environment around the Fe atom in the $[(C_5H_5)Fe(CO)_2]_2$ complex is similar to that around the Cr in this complex, it may be reasonable to compare the electronic structures as well as the $3d$ electron distributions of both metals. As for the Fe atom, six $3d$ electrons of Cr^0 will occupy the lower energy d_{z^2}, $d_{x^2-y^2}$, and d_{xy} orbitals, leaving d_{xz} and d_{yz} vacant (the z axis is taken parallel to the threefold axis of the complex, and the x and y perpendicular to this axis). This electronic structure will give rise to a similar aspherical distribution of $3d$ electrons to that in the vicinity of the Fe atom (Fig. 17a–d).

Accurate X-ray analyses have been carried out for the acentric crystals of $(\eta^5\text{-}C_5H_5Ni)_2C_2H_2$. As shown in Fig. 18 the diamagnetic binu-

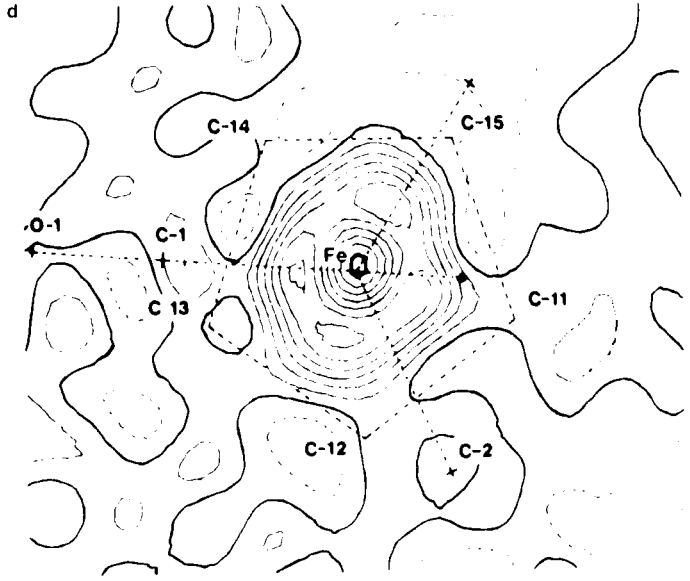

FIG. 17d (see legend p. 60).

clear complex contains a short Ni—Ni bond of 2.345(3) Å, being characterized by *mm* symmetry (one mirror plane along the Ni—Ni bond bisecting the acetylene bond, and the other containing the acetylene groups and bisecting the Ni—Ni bond). Each Ni atom is bridged by one acetylene group [Ni—C, 1.884(4) Å] and coordinated by the disordered cyclopentadienyl group (average Ni—C, 2.15 Å). The acetylene group is cis bent with a C—C distance of 1.341(6) Å, which is much longer than the triple bond distance and close to the C—C double bond distance (*36*).

The observed deformation density shows two large but slightly diffuse peaks of 1.0 e Å^{-3} in the vicinity of the Ni nucleus in the direction passing through a Ni atom and a center of C_5H_5 moiety. Although the direction of this excess $3d$ electron density may correspond to the excess density on the C_3 axis (d_{z^2} orbital) observed in $[(C_5H_5)Fe(CO)_2]_2$, the positive regions are spread out over the directions of Ni—Ni and Ni—C_2H_2 bonds. From the general aspect about $3d$ electron distribution, both the observed and theoretical deformation density in the vicinity of metal atom show positive peaks of $3d$ electrons in the directions of nonbonding or π bonding orbitals, and negative peaks in the directions of σ bondings. This feature of $3d$ electron distribution may correspond to the essentially nonbonding character of $3d$ orbitals. From this viewpoint, it may be expected that the deformation density

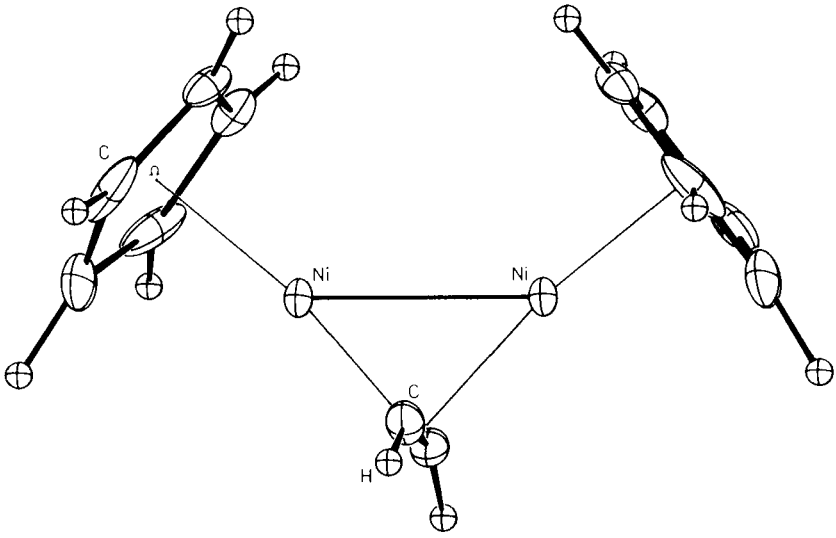

FIG. 18. Molecular structure of $(\eta^5\text{-}C_5H_5Ni)_2C_2H_2$.

might show negative peaks in the directions of the Ni—Ni and Ni—C_2H_2 bonds. Theoretical calculations for $(\eta^5\text{-}C_5H_5Ni)_2C_2H_2$ (*9b*) supports this expectation and is not consistent with the actual observation. This mysterious deformation density in crystals of $(\eta^5\text{-}C_5H_5Ni)_2C_2H_2$ may arise from some errors of crystallographic origin. The errors possibly originate from the noncentrosymmetric and disordered crystal structure of this complex. As noted in Section II,C, the former will lead to serious error in the observed deformation density owing to the large uncertainty of the phase angle for each reflection. Large thermal vibrations of the complex, which make the deformation density smeared out, should be taken into account.

IV. Net Charges of Transition Metal Atoms

Transition metals are characterized by their diversity of oxidation number. Generally the metal atom with high oxidation number does not bear a charge equal to its oxidation number but the charge is neutralized by donation of electrons from its neighboring atoms [Pauling's electroneutrality rule (*60*)]. Estimation of net (effective) charge is thus important for discussion of the metal–ligand bond nature as well as the chemical behavior of the molecule. Transition metal atoms are largely ionic in compounds such as metal silicates and oxides, whereas

they are mostly nearly neutral in transition metal complexes. In this latter case, metal d orbitals as well as originally unoccupied s and p orbitals are expected to overlap with σ and π orbitals of the ligating atoms. In molecular orbital representation, charge donation from the ligating groups to the metal atom corresponds to the construction of occupied bonding orbitals from originally unoccupied metal orbitals and occupied orbitals of the ligating groups. On the other hand, back donation means constructing molecular orbitals from occupied metal orbitals and unoccupied ligand orbitals. For complexes of transition metal atoms with high oxidation number, charge donation plays an important role for metal–ligand bond formation, while both the charge donation and back donation take place in organometallic compounds.

A. Estimation of Net Charges of Atoms

Two approaches have been applied to estimate the net charges of atoms from the observed electron-density distribution in crystals. The first method is a direct integration of observed density in an appropriate region around an atom (hereafter abbreviated as DI method) (*64*). The second is the so-called extended L-shell method (ELS method) (*19*, *81*) in which a valence electron population of an atom is calculated by a least-squares method on the observed and calculated structure amplitudes.

The number of electrons belonging to an atom is calculated by the integration of electron density in an effective region of the atom,

$$C = \int_{\substack{\text{effective} \\ \text{region}}} \rho(\mathbf{r}) dv \tag{12}$$

Since an a priori definition of the effective region is hardly possible, each atomic region is usually approximated by a spherical region around the atom, where the radius is taken as its ionic, atomic, or covalent bond radius. The radial distribution of electron density around an atom is also useful to estimate the effective radius of an atom, particularly in ionic crystals. In an ionic crystal, the distance from the metal nucleus to the minimum in the radial distribution curve generally corresponds to the ionic radius. As an example, the radial distribution curves around K^+ in α-K_2CrO_4 (*85*) are shown in Fig. 19a. The radial distributions of valence electrons ($2p$ electrons) exhibit a minimum at 1.60 Å for K(1) and 1.52 Å for K(2), respectively. These distances correspond to the ionic radii in crystals (1.52–1.65 Å)

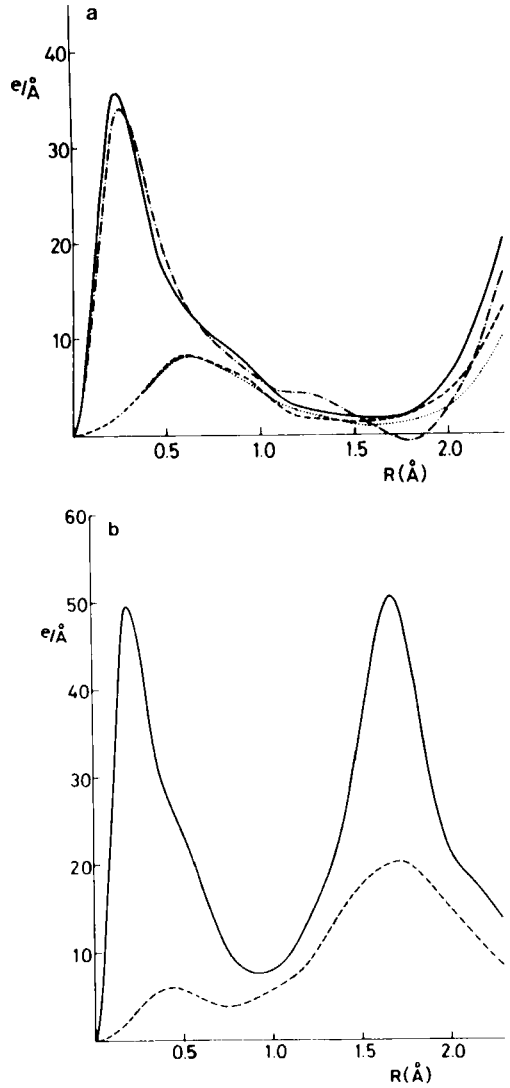

FIG. 19. Radial distributions of the electron density of α-K_2CrO_4 (*85*). (a) Observed values for total electrons (–·–·–) and valence electrons (·····) around the K-1 atoms, and for total electrons (——) and valence electrons (- - - - -) around the K-2 atom. (b) Observed values for total electrons (——) and valence electrons (- - - -) around the Cr atom.

(*36*). This method is occasionally hindered by difficulties in the case of highly covalent clusters such as CrO_4^{2-}. Figure 19b shows the radial distribution around the Cr atom, which seems to show no apparent radius of the Cr atom, because of marked superposition of the Cr and four bonded O atoms. When the net charge of an atom is estimated from the number of electrons included in each atomic region, the charge distributed outside in each atomic region hinders exact estimation of the net charge of the central metal atom.

In the case of α-K_2CrO_4, the estimation was carried out on a crude assumption that the interatomic charge could be assigned equally to the Cr and the four O atoms. Staudenmann *et al.* (*69*) have proposed a different method to define the effective region of an atom, where an atomic region is represented by an assembly of many small parallel piped volume elements for computational convenience. This method may enable us to define the effective atomic region more precisely for covalent molecules. From a practical point of view, however, it seems to be difficult to define an exact atomic region in this way.

In the ELS method, an additional parameter p is introduced in the least-squares calculation to obtain the population of valence electrons as follows:

$$f_{\text{total}} = f_{\text{core}} + pf_{\text{valence}} \tag{13}$$

where f_{total}, f_{core}, and f_{valence} stand for the atomic form factors of total, core, and valence electrons, respectively. Parameters, p, for all the atoms are determined by the least-squares fitting between observed and calculated structure amplitudes. Calculated structure amplitudes are directly related to p for each atom as shown in the modified equation of (*7*).

$$F_c = \sum_j (f_{\text{core}} + pf_{\text{valence}})_j T_j \exp[2\pi i(hx_j + ky_j + lz_j)] \tag{14}$$

Core and valence electrons can be divided based on a criterion of whether their distributions and populations are changed or not owing to bond formation. The electron population analysis conventionally uses spherical form factors, f, which are given by the spherically averaged Fourier transform of electron-density distributions.

This method may be useful to estimate the approximate net charge of atoms, because they are easily calculated by the conventional least-squares method. However, it seems that the ELS method does not necessarily yield accurate net charges of the atoms. The method is

based on the assumption that the spatial distribution of valence electrons remains unchanged by the bond formation and only their populations are changed. In practice, however, valence electron distributions may be compressed by the electrostatic field of bonding atoms in the region near the atomic nucleus (*16*) and expanded in the bonding region owing to the charge accumulation upon bond formation. Accordingly the net charge of an atom is not expected to be proportional to a number of valence electrons in the vicinity of the atomic nucleus, especially in molecular crystals. On the other hand, the ELS method may yield reasonable net charges of atoms in ionic crystals such as $CoAl_2O_4$ (*84*), because no charge accumulation occurs in the bonding region.

Two advanced techniques have been proposed and applied to some crystal structures (Section IV,C), in which aspherical distributions of valence electrons around an atom are directly taken into account in the least-squares calculations. Aspherical atomic form factors are introduced in the least-squares refinement in the first method (*29, 38, 80*) and multipole parameters describing the aspherical valence distributions are used in the second method (*31, 34, 46*).

B. Net Charges of Transition Metal Atoms

Net charges of transition metal atoms have been estimated by the methods described above for coordination compounds (*37, 59, 85*), organometallic compound (*63*), and minerals (*30, 65*). The results are summarized in Table III. The net charges of Co atoms in the coordination compounds are estimated by the DI method to be largely neutralized to $+0.2$–$+0.7$ compared to the formal oxidation number of $+3$ (*37, 59*). In organometallic compound such as $Cr(CO)_6$, the Cr atom also has a net charge practically equal to zero (*63*). It is remarkable that the Cr atom, having an oxidation number as high as $+6$, has been estimated by the DI method to possess the almost zero net charge of $+0.1(1)$ in the oxo anion CrO_4^{2-} (*85*). This result, however, may be somewhat doubtful because of the crude assumption described in the previous section. In fact, the ELS method gave the net charge of $+2.78(6)$ for the Cr atom, indicating some ionic character. Judging from the errors in both methods, the net charge of Cr(VI) may fall somewhere between two values, i.e., about $+1.0$. All the results suggest that the net charge of the transition metal atom is almost neutral but slightly positive in the complex. Highly neutralized net charges of transition metal atoms indeed verify Pauling's electroneutrality rule (*60*) for the transition metal complexes.

TABLE III

OBSERVED NET CHARGES OF TRANSITION METAL ATOMS

Metal	Net charge (DI method)	Radius (Å)[a]	Net charge (ELS method)	Oxidation number	Compound	Reference
Co	+0.7(1)	1.22	+0.06(6)	+3	$[Co(NO_2)_6]^{3-}$	*59*
Co	+0.7(3)	1.22	+0.8(1)	+3	$[Co(NH_3)_6]^{3+}$	*37*
Co	+0.2(3)	1.22	+0.4(1)	+3	$[Co(CN)_6]^{3-}$	*37*
Cr	+0.15(12)			0	$Cr(CO)_6$	*63*
Cr	+0.1(1)	0.97+[b]	+2.78(6)	+6	CrO_4^{2-}	*85*
Co			+1.5(1)	+2	$CoAl_2O_4$	*84*
Mn	+1.58(1)	1.15		+2	MnO	*65*
Mn	+1.21(6), +1.49(6)	1.15		+2	Mn_2SiO_4	*65*
Fe	+0.85(8), +1.54(7)	1.11	+1.3(1), +1.9(1)	+2	α-Fe_2SiO_4	*30*
Mn	+1.21(6), +1.49(6)	1.15	+1.3(1), +2.2(2)	+2	α-Mn_2SiO_4	*30*

[a] Radius of sphere defining the effective atomic region, electron density being integrated in this sphere.

[b] One-fifth of electrons in the interatomic region (region out of each atomic region) being added.

In order to analyze the charge distribution in a complex, electron population analyses have been carried out for the complexes $[Co(NO_2)_6]^{3-}$, CrO_4^{2-}, and $Cr(CO)_6$. Applying the ELS method to $[Co(NO_2)_6]^{3-}$, the net charges of Co, N, and O atoms were estimated to be +0.06(6), −0.07, and −0.22(2) *e*, respectively (*59*). The charge distribution in CrO_4^{2-} was calculated by the DI method as +0.1 for Cr and −0.5(1) for O atoms (*85*). For $Cr(CO)_6$, the following net charges were estimated by the DI method (*63*): Cr, 0.15(12); C, 0.09(5); and O, −0.12(5) *e*. As seen from these results, the charge of the complex ion is not concentrated on the transition metal atom but distributed all over the atoms in the complex, where effective charges of atoms may depend on their electronegativities.

In metal oxides and silicates, the net charges of transition metal atoms are quite different. Table III shows the net charges of metal atoms in these crystals, which are slightly neutralized but almost equal to their oxidation numbers. The ionic characters of these crystals may be demonstrated by the electron population analysis of the $CoAl_2O_4$ crystal. The net charges of Co(II), Al(III), and O(II) atoms were estimated by the ELS method to be +1.5(1), +2.8(1), and −1.8 *e*, respectively (*84*).

TABLE IV

ELECTRON POPULATIONS IN 3*d* ATOMIC ORBITALS SPLIT IN A D_{3d} LIGAND FIELD

Complex	Metal	a_{1g}	e_g'	e_g	4*s*	Reference
FeS_2	Fe^{2+}	2.0(1) [2][a]	3.2(1) [4]	0.8(2) [0]		*75*
$[Cr(CN)_6]^{3-}$ (80 K)[b]	Cr^{3+}	1.0(6) [1]	2.4(2) [2]	2.2(12) [0]		*38*
$[Co(CN)_6]^{3-}$ (298 K)	Co^{3+}	1.9(3) [2]	4.3(5) [4]	3.2(6) [0]		*38*
$[Co(NH_3)_6]^{3+}$ (80 K)	Co^{3+}	1.3(7) [2]	4.6(15) [4]	3.0(10) [0]		*38*
$[Co(NH_3)_6]^{3+}$ (298 K)	Co^{3+}	1.8(3) [2]	4.5(6) [4]	3.2(5) [0]		*38*
$Cr(CO)_6$	Cr^0	3.8		1.2	1	*63*
		4.5		1.5	0	*63*

[a] Number of 3*d* electrons expected from a simple crystal field model.
[b] Experimental temperature in reflection data measurement.

C. 3*d* ELECTRON POPULATIONS IN EACH ATOMIC ORBITAL PLACED IN A LIGAND FIELD

By introducing aspherical atomic form factors for 3*d* atomic orbitals of a transition metal atom in a ligand field, populations in each orbital can be determined. This method has been applied to four crystals: $[Co(NH_3)_6][Co(CN)_6]$ (*37*), $[Co(NH_3)_6][Cr(CN)_6]$ (*38*), $Cr(CO)_6$ (*63*), and FeS_2 (*75*). The number of 3*d* electrons in each atomic orbital is successfully estimated by this method, and is listed in Table IV, along with the number of 3*d* electrons expected from the crystal field model. It is interesting that 3*d* electrons significantly occupy an originally vacant e_g orbital, whose nature is essentially antibonding. These results cannot be interpreted on the basis of the crystal field model. In molecular orbital representation, however, higher energy e_g orbitals of a transition metal atom will be mixed with the bonding orbitals of ligating atoms and give rise to both lower energy bonding and higher energy antibonding orbitals. The bonding orbitals are doubly occupied in these complexes. Consequently, the 3*d* electron population in an e_g orbital may correspond to the extent of its contribution to the bonding orbital. This interpretation seems to be supported by the highly neutralized net charges of transition metal atoms and the positions of observed bonding peaks, which will be discussed in Section V,B. No further quantitative discussion can be made owing to insufficient accuracy.

D. Formal Oxidation States of Transition Metal Atoms

It is well known that transition metal atoms take characteristic stereo-structures corresponding to their formal oxidation numbers. As mentioned in Section IV,B, however, all the net charges of transition metal atoms in various complexes are found to be highly neutralized, and appear to give similar values regardless of their oxidation numbers. The oxidation number of a transition metal atom is also unidentifiable from the observed deformation density around the atom. Electron-density distributions around the metal atoms having different oxidation numbers are known for Co, Cr, and Fe complexes in the following crystals: Co(III), $K_2Na[Co(NO_2)_6]$, $[Co(NH_3)_6][Co(CN)_6]$; Co(II), $CoAl_2O_4$, γ-Co_2SiO_4, and $KCoF_3$; Cr(VI), α-K_2CrO_4; Cr(III), $[Co(NH_3)_6][Cr(CN)_6]$; Cr(0), $Cr(CO)_6$; Fe(II), FeS_2, γ-Fe_2SiO_4; Fe(I), $[(C_5H_5)Fe(CO)_2]_2$. Comparing these observed deformation densities for a particular metal, they apparently vary from one compound to another, and depend on a number of factors such as the symmetry of the ligand field, its field strength, the bonding nature, and the formal oxidation numbers of the atoms. Electron-density distributions around the Co(II) differ drastically between the tetrahedral environment in the $CoAl_2O_4$ crystal and the trigonally deformed octahedral environment in γ-Co_2SiO_4, as crystal field theory predicts. Depending on the ligand field strength around the transition metal atom, its spin state, or electronic structure changes, Fe(II) takes a low-spin state in the crystals of FeS_2 and a high-spin state in γ-Fe_2SiO_4. No features directly related to the oxidation state could be detected on the observed deformation density maps, probably because deformation due to bond formation would mask them. Despite the fact that the Cr atom in $Cr(CO)_6$ has a lower oxidation number of 0 compared with +3 in $[Cr(CN)_6]^{3-}$, the asphericity observed in $Cr(CO)_6$ is smaller than that in $[Cr(CN)_6]^{3-}$.

On the other hand, the difference in the number of $3d$ electrons on the transition metal atoms is clearly distinguishable in the series of studies of γ-M_2SiO_4 (M = Fe, Co, Ni) and KMF_3 (M = Mn, Co, Ni) (Section III,A,1). In these ionic crystals, the environments around the metals have similar octahedral symmetry, and their ligand field strengths are all weak. As discussed in Section III,A,1, aspherical distributions of $3d$ electrons differ significantly each other, and correspond well to their different number of $3d$ electrons. It is to be noted that these differences are recognized in the vicinities of the transition metal atomic nuclei.

To sum up, neither the observed net charges nor the deformation densities give any useful information to distinguish oxidation states in transition metal complexes at the present stage. This must, of course, arise from the insufficient accuracy of the observed electron densities.

V. Chemical Bonds between Transition Metal Atoms and Ligating Atoms

It is essential to elucidate the nature of the chemical bond between a transition metal atom and the ligating atoms for a deeper understanding of the chemical properties of transition metal compounds. Electron-density distributions have been observed in various types of crystals involving the ionic, coordination, and covalent bonds in which a transition metal atom participates in the bond formation. Observed deformation densities around these bonds show different pictures reflecting the bond natures. They are generally consistent with the classical bond models of ionic, coordination, and covalent bonds. Furthermore, it has also become apparent that the chemical bonds involving transition metal atoms differ significantly in the manner of charge accumulation upon bond formation, in contrast to the bonds between the first-row atoms (*14, 20*). The piling up of charge is more diffuse in magnitude and takes place in the region distant from metal nuclei.

A. Ionic Bonds

Ionic bonds containing transition metal atoms have been studied in crystals such as oxides, silicates, and fluorides. The most typical ionic bond can be demonstrated by the Co—O bond in $CoAl_2O_4$ (Fig. 5). The normal spinel crystal of $CoAl_2O_4$ can be regarded as essentially ionic on the basis of the net charges of the constituent atoms (Section IV,B). The deformation density around the Co—O ionic bond shows no positive peak on the bond axis, except for the positive peak at a distance of 0.3 Å from the O nucleus. This may be attributed to the lone-pair electrons, although a possibility of an artifact owing to a positional disorder between Co and Al atoms in each site can by no means be excluded. Positive peaks attributable to the lone-pair electrons generally appear at distances ranging from 0.3 to 0.4 Å from the atomic nuclei in organic compounds (*20*).

On the other hand, a negative peak is observed on the bond axis in the vicinity of the Co nucleus, which can be attributed to the aspherical distribution of $3d$ electron density (Section III,A,1). This negative peak indicates the deficiency of $3d$ electron density on the bond axis, in

other words, the charge migration occurs by electrostatic field of O^2 in such a way that the charge avoids the region of high field due to the oxide ions. Similar features have been observed in other deformation densities in crystals containing transition metal ionic bonds. Particular charge migration and/or piling up can be hardly observed on a line joining both ions.

B. Coordination Bonds

In transition metal complexes, the chemical bond between a transition metal atom and a first-row or sulfur atom can be described in terms of a coordination bond. The coordination bond is formally described as the donation of lone-pair electrons of a ligating atom to the transition metal atom. When such bonds are formed, the spectroscopic and magnetic properties of the complexes are primarily interpreted on the basis of the electronic structure in $3d$ atomic orbitals, where the energy levels split into lower t_{2g} and higher e_g orbitals in the electrostatic field exerted by the ligating atoms around the central metal atom. More exact descriptions for the coordination bond may be made by employing molecular orbitals, where significant overlaps between transition metal and ligating atomic orbitals occur along with the essentially lone-pair character of the bonding orbitals.

Observed deformation densities of the transition metal complexes provide some interesting information on the coordination bond. Electron-density distribution in $[Co(NH_3)_6][Co(CN)_6]$, which contains some of the most familiar coordination bonds, Co—NH_3 and Co—CN, is presented in Fig. 20. Remarkable positive peaks appear on the Co—N and Co—C bond axes, which should be attributed to the bonding electrons analogous to the C—C bonding electrons observed in a number of hydrocarbon molecules. Comparing the deformation densities around the coordination bonds with those around the C—C covalent bonds (*20*), the distribution of the positive and negative peaks in the vicinity of the transition metal atoms differs remarkably. The charge accumulation on bond formation does not take place at the center of the bond but nearer to the ligating atom: positive peaks are at 0.6 Å from N and C atoms in Co—NH_3 and Co—CN bonds, respectively (heteronuclear bonds). In covalent bonds, these positive peaks are shifted toward the bond center. Closer examination shows slight differences in the distance between the ligating atomic nucleus and the positive peak: 0.52 Å in Co—NO_2 (Fig. 1) and 0.5 Å for Cr—CO (Fig. 15).

Poor accuracy does not, however, permit further discussion. The shapes of the positive peaks on coordination bond axes seem to reflect

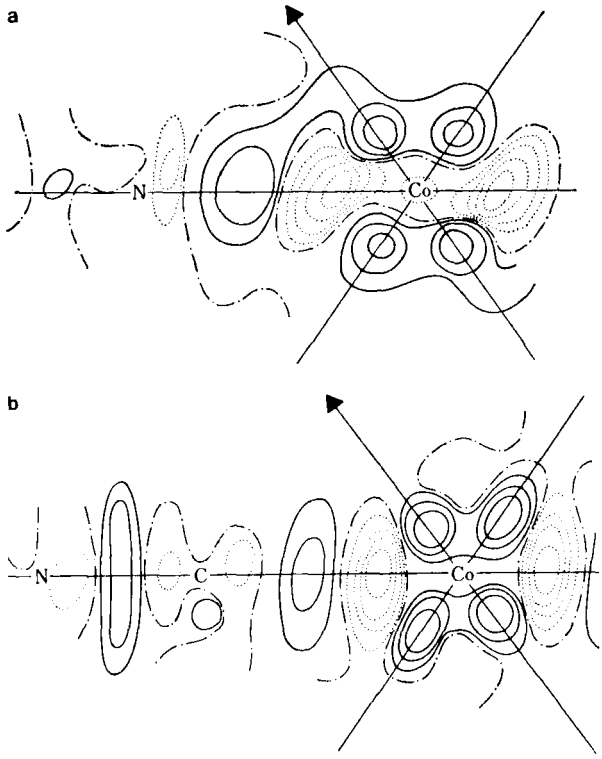

FIG. 20. Deformation density of $[Co(NH_3)_6][Co(CN)_6]$ (37). Contours are at intervals of 0.1 e Å^{-3}. (a) A section through a Co—NH_3 bond and a C_3 axis. (b) A section through a Co—CN bond and a C_3 axis.

the nature of the bonds. As shown in Fig. 20, the positive peak on the Co—NH_3 axis is spherical in contrast to the Co—CN bonding peak of an ellipsoidal form extending perpendicularly to the bond axis. This indicates the π-back bonding character of the Co—CN bond. A similar feature of charge accumulation due to back bonding is more clearly presented in the observed deformation density of $Cr(CO)_6$ (Fig. 15). Bonding features of the Cr—CO bond are interpreted as the back donation of excess charge on the Cr atom to CO groups along with the σ-type donation from the CO to the Cr atom. Back bonding molecular orbitals with π-character are formed by a mixing of nonbonding e_g ($3d$) orbitals of the Cr atom with π-bonding orbitals of CO molecules. The observed deformation density around the Cr—C bond seems to confirm the bonding manner described above. A similar trend can also be observed in the Co—NO_2 bond of $[Co(NO_2)_6]^{3-}$.

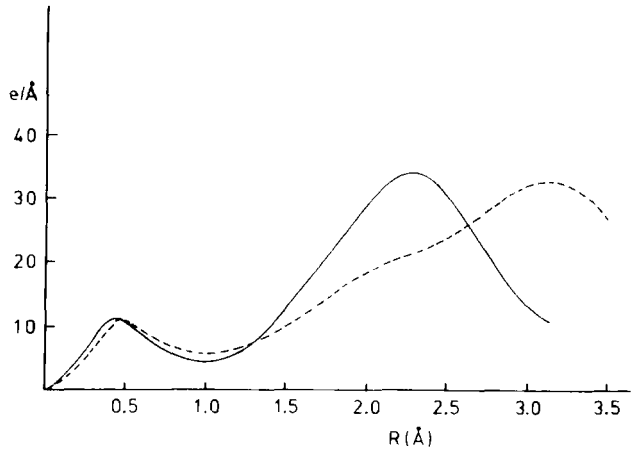

FIG. 21. Radial distribution of the valence electron density around the Co atom in $[Co(NH_3)_6][Co(CN)_6]$ crystal (*37*). Observed values for $[Co(NH_3)_6]^{3+}$ (——) and $[Co(CN)_6]^{3}$ (- - - - -).

Radial electron density distributions around the transition metal atoms has been calculated from the observed electron density in the crystals of $[Co(NH_3)_6][Co(CN)_6]$ (*37*). Figure 21 shows the observed radial distribution of valence electrons ($3d$ for Co, and $2s$ and $2p$ for N and C atoms), from which no particular charge accumulation can be detected in the bonding regions. Conversely, it may be noted that only a small amount of piling up of charge density, that cannot be detected in this type of analysis, takes place on bond formation. As seen from Fig. 21, however, the curve shows significant overlap of the metal valence orbitals and ligand orbitals. Both observed net charges of the transition metal atoms (Table III) and partially occupied e_g orbitals (Table IV) correspond well to the significant overlap of these orbitals on forming coordination bonds. The positional shifts of positive peaks on bond axes, which are still included in the effective region of the ligating atom, can be interpreted in terms of the bonding molecular orbital formation. To sum up, a coordination bond involving $3d$ transition elements is constructed by the significant overlap of $3d$ and $4s$ atomic orbitals of a metal atom with ligating atomic orbitals, i.e., the charge is donated from the ligating atom to the central metal atom.

C. Covalent Bonds

Figure 19b presents the observed radial distribution of valence electrons around the Cr atom in the crystals of α-K_2CrO_4. As shown in the

figure, a remarkable positive radial density can be seen in the bonding region, corresponding to the short Cr—O bond of 1.646(1) Å. The observed deformation density (Fig. 6) around the Cr—O bond shows a feature similar to that of the coordination bond; a positive peak is located near a ligating O atom and a negative peak in the vicinity of a Cr atom on the Cr—O bond axis. Beside these similarities, the deformation density is somewhat different. The positive peaks are located further apart from the ligating atom than those of the coordination bond, migrating to the bond center (0.7 Å from the O atom). Consequently, it is reasonable to assume the multiple valency for the Cr—O bond in this transition metal oxo anion.

D. Chemical Bonds in π-Complexes

Only one reliable deformation density map of this type of the bond has been reported, for the $[(C_5H_5)Fe(CO)_2]_2$ crystal (*52*). The detailed analysis has already been described in Section III,C. An investigation on the charge accumulation upon Fe—C_5H_5 bond formation was carried out; however, no significant positive peak of bonding electrons could be observed in the deformation density map around the bond (Fig. 17a). The piling up of charge density due to bond formation may hardly occur in this type of bond. This fact seems to reflect the diffuse character of both the π bonding orbitals of the cyclopentadienyl moiety and the $4s$ and $3d$ atomic orbitals of the Fe atom.

VI. Electron-Density Distributions in Some Inorganic Crystals

Single crystal X-ray diffraction measurements have been successfully applied to the observations of electron distributions in a number of inorganic crystals, such as metals, nonmetals, and inorganic salts involving alkali and/or simple ions. Some interesting references are listed in Table V. Because of a limited space available, only results for metals will be discussed here.

Aspherical Electron Distribution in Metal Crystals

Since Weiss and DeMarco (*91*) detected the asphericity in charge distribution in vanadium metal, the $3d$ electron distributions in crystals of V, Cr, and Fe have been studied experimentally as well as theoretically (*89*). Crystals of V, Cr, and Fe are body-centered cubic at room temperature and under normal pressure. Charge asphericity has

TABLE V

SOME SELECTED REFERENCES ON ELECTRON-DENSITY MEASUREMENTS IN CRYSTALS OF INORGANIC COMPOUNDS AND METALS

Crystal	Space group	Reference
$NaCN \cdot 2H_2O$	$P2_1/c$	3
NaSCN	$Pmcn$	7
NH_4SCN	$P2_1/c$	5
$NaClO_4 \cdot H_2O$	$C2/c$	48
NH_4ClO_4	$Pnma$	47
$CaSO_4$	$Amma$	46
H_3NSO_3	$Pbca$	6
$NH_2C_6H_4SO_3Na \cdot 2H_2O$	$Pbca$	4
$Na_2S_2O_6 \cdot 2H_2O$	$Pnma$	45
NaN_3	$R\bar{3}m$	76, 77
KN_3	$I4/mcm$	71, 77
S_8	$Fddd$	22
$S_4N_3 \cdot NO_3$	$P2_1/n$	54
$B_{13}C_2$	$R\bar{3}m$	44
H_2O_2	$P4_12_12$	66
Si	$Fd\bar{3}m$	67
V_3Si	$Pm\bar{3}n$	69
V	$Im\bar{3}m$	58
Cr	$Im\bar{3}m$	57
Fe	$Im\bar{3}m$	56

been conventionally estimated by comparing the intensity ratios of the paired reflections having the same sin θ/λ value: if the charge distribution around the atom is spherically symmetric, their intensities depend only on the thermal vibrations of the atom and are the same. In recent years, accurate single crystal measurements have been carried out for the crystals of V, Cr, and Fe (*56*, *57*, *58*), and aspherical charge distributions were detected on the difference maps. Figure 22a shows a section of the deformation density of Cr parallel to the (110) plane. The electron excess region has a maximum peak in the [111] direction, being identical to the direction to a nearest neighboring atom. In all, eight equivalent peaks are arranged at the apices of a cube around the Cr atom and they are linked together with a high electron density region. The peak height is 1.4(1) e Å^{-3} and the peak lies at 0.25 Å from the nucleus. A theoretical valence electron density map of the same plane computed from the band calculation based on the augmented plane wave method is presented in Fig. 22b (*57*). Peaks of 5.8 e Å^{-3} are found on the [111] axis at 0.23 Å from the nucleus. The theoretical

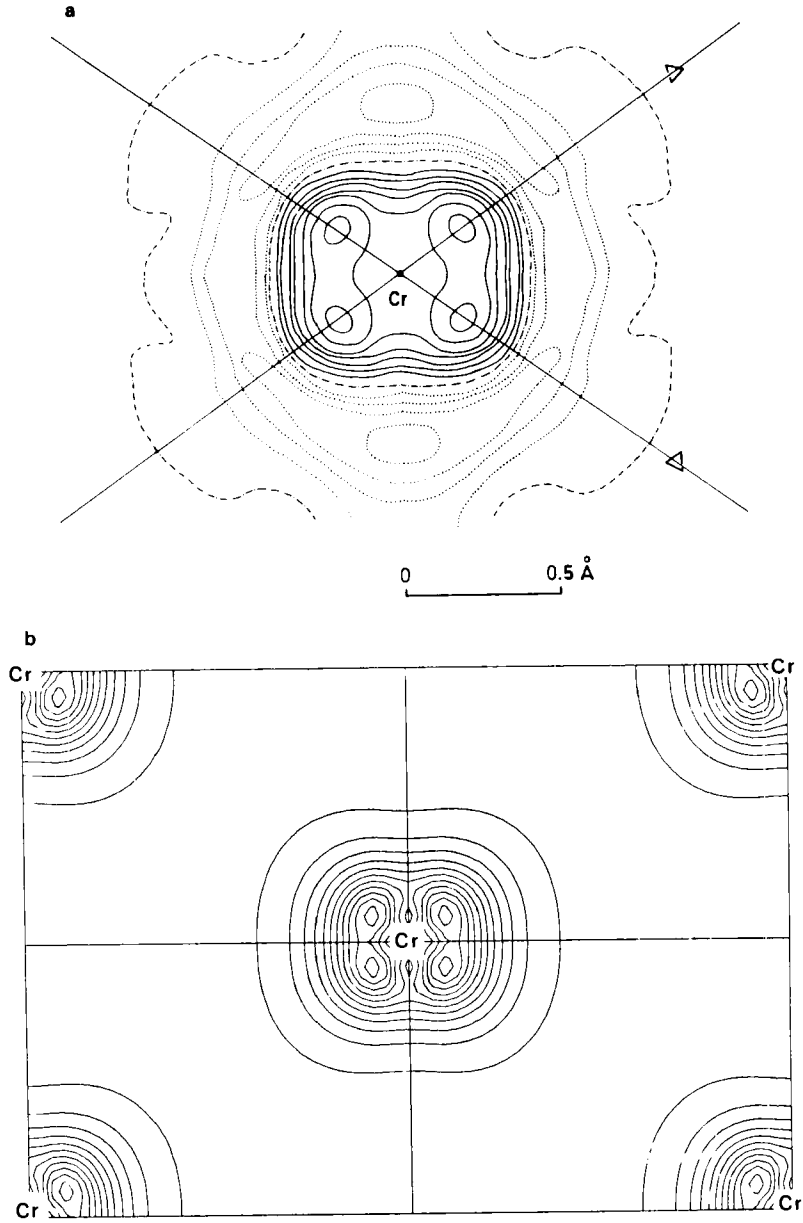

FIG. 22. Deformation densities of a Cr metal in a section through the Cr atom and parallel to the (110) plane (57). (a) Observed map. Contours are at intervals of 0.2 e Å^{-3}. (b) Theoretical map. Contours are drawn at 0.5 e Å^{-3} intervals.

results show that the observed charge asphericity is due to $3d$ electrons in t_{2g} orbitals in O_h environment.

By the method of Weiss and DeMarco (*91*), the t_{2g} orbital populations were estimated to be 0.666(28), 0.670(23), and 0.648(14) for V, Cr, and Fe, respectively, indicating excess electrons in t_{2g} orbitals.

VII. Concluding Remarks

Measurement of electron density by X-ray diffraction cannot distinguish each electron in different orbitals; however, it provides overall information on the asphericity of the d electron distribution in a molecule as well as on the redistribution of electrons upon chemical bond formation. At the present stage, experimental charge distributions can be compared only qualitatively with theoretical calculations. The method, however, will be of considerable value in clarifying poorly understood bonding situations. If the electron-density distribution and the geometrical arrangement of the atomic nuclei in a complex are known, it is possible, at least in principle, to predict all its physical and chemical properties on the basis of quantum mechanics.

ACKNOWLEDGMENT

The authors would like to thank Dr. Kazuo Kitaura for his valuable suggestions concerning molecular orbital interpretations. The authors are, however, entirely responsible for the content of this article.

REFERENCES

1. Abrahams, S. C., *Acta Crystallogr. Sect. A* **25,** 165 (1969).
2. Baerends, E. J., and Ros, P., *Mol. Phys.* **30,** 1735 (1975).
3. Bats, J. W., *Acta Crystallogr. Sect. B* **33,** 466 (1977).
4. Bats, J. W., *Acta Crystallogr. Sect. B* **33,** 2035 (1977).
5. Bats, J. W., and Coppens, P., *Acta Crystallogr. Sect. B* **33,** 1542 (1977).
6. Bats, J. W., Coppens P., and Koetzle, T. F., *Acta Crystallogr. Sect. B* **33,** 37 (1977).
7. Bats, J. W., Coppens, P., and Kvick, Å., *Acta Crystallogr. Sect. B* **33,** 1534 (1977).
8. Becker, P. J., and Coppens, P., *Acta Crystallogr. Sect. A* **30,** 129 (1974).
9a. Bénard, M., *J. Am. Chem. Soc.* **100,** 2354 (1978).
9b. Bénard, M., personal communication.
10. Bénard, M., Coppens, P., DeLucia, M. L., and Stevens, E. D., *Inorg. Chem.* **19,** 1924 (1980).
11. Bohn, R. K., and Haaland, A., *J. Organomet. Chem.* **5,** 470 (1966).
12. Coleman, J. M., and Dahl, L. F., *J. Am. Chem. Soc.* **89,** 542 (1967).
13. Coppens, P., *Acta Crystallogr. Sect. B* **30,** 255 (1974).

14. Coppens, P., *Angew. Chem. Int. Ed. Engl.* **16,** 32 (1977).
15. Coppens, P., and Coulson, C. A., *Acta Crystallogr.* **23,** 718 (1967).
16. Coppens, P., Guru Row, T. N., Leung, P., Stevens, E. D., Becker, P. J., and Yang, Y. W., *Acta Crystallogr. Sect. A* **35,** 63 (1979).
17. Coppens, P., and Hamilton, W. C., *Acta Crystallogr. Sect. B* **24,** 925 (1968).
18. Coppens, P., and Hamilton, W. C., *Acta Crystallogr. Sect. A* **26,** 71 (1970).
19. Coppens, P., Pautler, D., and Griffin, J. F., *J. Am. Chem. Soc.* **93,** 1051 (1971).
20. Coppens, P., and Stevens, E. D., *Adv. Quantum Chem.* **10,** 1 (1977).
21. Coppens, P., and Vos, A., *Acta Crystallogr. Sect. B* **27,** 146 (1971).
22. Coppens, P., Yang, Y. W., Blessing, R. H., Cooper, W. F., and Larsen, F. K., *J. Am. Chem. Soc.* **99,** 760 (1977).
23. Cotton, F. A., DeBoer, B. G., LaPrade, M. D., Pipal, J. R., and Ucko, D. A., *Acta Crystallogr. Sect. B* **27,** 1664 (1971).
24. Cotton, F. A., Mester, Z. C., and Webb, T. R., *Acta Crystallogr. Sect. B* **30,** 2768 (1974).
25. Cotton, F. A., and Harris, C. B., *Inorg. Chem.* **4,** 330 (1965).
26. Cruickshank, D. W. J., *Acta Crystallogr.* **2,** 65 (1949).
27. Cruickshank, D. W. J., and Rollett, J. S., *Acta Crystallogr.* **6,** 705 (1953).
28. Dawson, B., *Acta Crystallogr.* **17,** 990 (1964).
29. Dawson, B., *Acta Crystallogr.* **17,** 997 (1964).
30. Fujino, K., Sasaki, S., Takéuchi, Y., and Sadanaga, R., *Acta Crystallogr. Sect. B* **37,** 513 (1981).
31. Harel, M., and Hirshfeld, F. L., *Acta Crystallogr. Sect. B* **31,** 162 (1975).
32. Hillier, I. H., and Saunders, V. R., *Mol. Phys.* **22,** 1025 (1971).
33. Hino, K., Saito, Y., and Bénard, M., *Acta Crystallogr. Sect. B* **37,** 2164 (1981).
34. Hirshfeld, F. L., *Acta Crystallogr. Sect. B* **27,** 769 (1971).
35. Hirshfeld, F. L., and Rzotkiewicz, S., *Mol. Phys.* **27,** 1319 (1974).
36. "International Tables for X-ray Crystallography," Vol. III, Kynoch Press, Birmingham, 1962.
37. Iwata, M., and Saito, Y., *Acta Crystallogr. Sect. B* **29,** 822 (1973).
38. Iwata, M., *Acta Crystallogr. Sect. B* **33,** 59 (1977).
39. Johansen, H., *Acta Crystallogr. Sect. A* **32,** 353 (1976).
40. Johnson, K. H., and Smith, F. C., Jr., *Phys. Rev. Sect. B* **5,** 831 (1972).
41. Kijima, N., Tanaka, K., and Marumo, F., *Acta Crystallogr. Sect. B* **37,** 545 (1981).
42. Kijima, N., Tanaka, K., and Marumo, F., *Acta Crystallogr. Sect. B* **39** (in press).
44. Kirfel, A., Gupta, A., and Will, G., *Acta Crystallogr. Sect. B* **36,** 1311 (1980).
45. Kirfel, A., and Will, G., *Acta Crystallogr. Sect. B* **36,** 512 (1980).
46. Kirfel, A., and Will, G., *Acta Crystallogr. Sect. B* **37,** 525 (1981).
47. Lundgren, J.-O., *Acta Crystallogr. Sect. B* **35,** 1027 (1979).
48. Lundgren, J.-O., *Acta Crystallogr. Sect. B* **36,** 1774 (1980).
49. Marumo, F., Isobe, M., Saito, Y., Yagi, T., and Akimoto, S., *Acta Crystallogr. Sect. B* **30,** 1904 (1974).
50. Marumo, F., Isobe, M., and Akimoto, S., *Acta Crystallogr. Sect. B* **33,** 713 (1977).
51. Maslen, E. N., *Acta Crystallogr. Sect. B* **24,** 1172 (1968).
52. Mitschler, A., Rees, B., and Lehmann, M. S., *J. Am. Chem. Soc.* **100,** 3390 (1978).
53. Miyamae, H., Sato, S., and Saito, Y., *Acta Crystallogr. Sect. B* **33,** 3391 (1977).
54. Moss, G., Guru Row, T. N., and Coppens, P., *Inorg. Chem.* **19,** 2396 (1980).
55. Ohba, S., Thesis, University of Tokyo (1980).
56. Ohba, S., Saito, Y., and Noda, Y., *Acta Crystallogr. Sect. A* **38,** 725 (1982).
57. Ohba, S., Saito, Y., and Wakoh, S., *Acta Crystallogr. Sect. A* **38,** 103 (1982).

58. Ohba, S., Sato, S., and Saito, Y., *Acta Crystallogr. Sect. A* **37,** 697 (1981).
59. Ohba, S., Toriumi, K., Sato, S., and Saito, Y., *Acta Crystallogr. Sect. B* **34,** 3535 (1978).
60. Pauling, L., "The Nature of Chemical Bond," 3rd ed., Cornell Univ. Press, Ithaca, New York, 1960.
61. Rees, B., *Acta Crystallogr. Sect. A* **32,** 483 (1976).
62. Rees, B., and Coppens, P., *Acta Crystallogr. Sect. B* **29,** 2516 (1973).
63. Rees, B., and Mitschler, A., *J. Am. Chem. Soc.* **98,** 7918 (1976).
64. Sakurai, T., *Acta Crystallogr.* **19,** 320 (1965).
65. Sasaki, S., Fujino, K., Takéuchi, Y., and Sadanaga, R., *Acta Crystallogr. Sect. A* **36,** 904 (1980).
66. Savariault, J.-M., and Lehmann, M. S., *J. Am. Chem. Soc.* **102,** 1298 (1980).
67. Scheringer, C., *Acta Crystallogr. Sect. A* **36,** 205 (1980).
68. Shintani, H., Sato, S., and Saito, Y., *Acta Crystallogr. Sect. B* **31,** 1981 (1975).
69. Staudenmann, J.-L., Coppens, P., and Muller, J., *Solid State Commun.* **19,** 29 (1976).
70. Stevens, E. D., *Acta Crystallogr. Sect. A* **30,** 184 (1974).
71. Stevens, E. D., *Acta Crystallogr. Sect. A* **33,** 580 (1977).
72. Stevens, E. D., and Coppens, P., *Acta Crystallogr. Sect. A* **31,** 612 (1975).
73. Stevens, E. D., and Coppens, P., *Acta Crystallogr. Sect. A* **32,** 915 (1976).
74. Stevens, E. D., and Coppens, P., *Acta Crystallogr. Sect. A* **35,** 536 (1979).
75. Stevens, E. D., DeLucia, M. L., and Coppens, P., *Inorg. Chem.* **19,** 813 (1980).
76. Stevens, E. D., and Hope, H., *Acta Crystallogr. Sect. A* **33,** 723 (1977).
77. Stevens, E. D., Rys, J., and Coppens, P., *Acta Crystallogr. Sect. A* **33,** 333 (1977).
78. Stewart, R. F., *Acta Crystallogr. Sect. A* **24,** 497 (1968).
79. Stewart, R. F., *J. Chem. Phys.* **48,** 4882 (1968).
80. Stewart, R. F., *J. Chem. Phys.* **51,** 4569 (1969).
81. Stewart, R. F., *J. Chem. Phys.* **53,** 205 (1970).
82. Tanaka, K., Konishi, M., and Marumo, F., *Acta Crystallogr. Sect. B* **35,** 1303 (1979).
83. Tanaka, K., and Saito, Y., *Acta Crystallogr. Sect. A* **31,** 841 (1975).
84. Toriumi, K., Ozima, M., Akaogi, M., and Saito, Y., *Acta Crystallogr. Sect. B* **34,** 1093 (1978).
85. Toriumi, K., and Saito, Y., *Acta Crystallogr. Sect. B* **34,** 3149 (1978).
86. Van Niekerk, J. N., Schoening, F. R. L., and de Wet, J. F., *Acta Crystallogr.* **6,** 501 (1953).
87. Vincent, M. G., Yvon, K., and Ashkenazi, J., *Acta Crystallogr. Sect. A* **36,** 808 (1980).
88. Vincent, M. G., Yvon, K., Grüttner, A., and Ashkenazi, J., *Acta Crystallogr. Sect. A* **36,** 803 (1980).
89. Wakoh, S., and Kubo, Y., *J. Phys. F* **10,** 2707 (1980).
90. Wang, Y., and Coppens, P., *Inorg. Chem.* **15,** 1122 (1976).
91. Weiss, R. J., and DeMarco, J. J., *Phys. Rev.* **140,** A 1223 (1965).
92. Wilson, A. J. C., *Acta Crystallogr. Sect. A* **35,** 122 (1979).
93. Woolfson, M. M., "An Introduction to X-ray Crystallography." Cambridge Univ. Press, London and New York, 1970.
94. Zachariasen, W. H., *Acta Crystallogr.* **23,** 558 (1967).